Scoping assessment of free-field vibrations due to railway traffic

P. Galvín[a,*], D. López Mendoza[a], D.P. Connolly[b], G. Degrande[c], G. Lombaert[c], A. Romero[a]

[a] *Escuela Técnica Superior de Ingeniería, Universidad de Sevilla, Camino de los Descubrimientos s/n, 41092 Sevilla, Spain*
[b] *Institute for High Speed Rail, Leeds University, LS2 9JT Leeds, UK*
[c] *Department of Civil Engineering, K.U.Leuven, Kasteelpark Arenberg 40, B-3001 Leuven, Belgium*

Abstract

The number of railway lines both operational and under construction is growing rapidly, leading to an increase in the number of buildings adversely affected by ground-borne vibration (e.g. shaking and indoor noise). Post-construction mitigation measures are expensive, thus driving the need for early stage prediction, during project planning/development phases. To achieve this, scoping models (i.e. desktop studies) are used to assess long stretches of track quickly, in absence of detailed design information. This paper presents a new, highly customisable scoping model, which can analyse the effect of detailed changes to train, track and soil on ground vibration levels. The methodology considers soil stiffness and the combination of both the dynamic and static forces generated due to train passage. It has low computational cost and can predict free-field vibration levels in accordance with the most common international standards. The model uses the direct stiffness method to compute the soil Green's function, and a novel two-and-a-half dimensional (2.5D) finite element strategy for train-track interaction. The soil Green's function is modulated using a neural network (NN) procedure to remove the need for the time consuming computation of track-soil coupling. This modulation factor combined with the new train-track approach results in a large reduction in computational time. The proposed model is validated by comparing track receptance, free-field mobility and soil vibration with both field experiments and a more comprehensive 2.5D combined finite element-boundary element (FEM-BEM) model. A sensitivity analysis is undertaken and it is shown that track type, soil properties and train speed have a dominant effect on ground vibration levels. Finally, the possibility of using average shear wave velocity introduced for seismic site response analysis to predict vibration levels is investigated and shown to be reasonable for certain smooth stratigraphy's.

Keywords: Scoping assessment, Free-field vibrations, Soil vibrations, Neural network, V_{s30} profile, Railroad vibration, Railway traffic, High speed rail, Ground-borne vibrations, Environmental Impact Assessment (EIA)

1. Introduction

The emergence of high speed rail (HSR) has stimulated economic development in Europe, America and Asia. This has also caused an increasing number of properties and structures affected by ground-borne railway vibrations [1]. International standard ISO2631 [2, 3] addresses these negative effects and evaluates the whole-body human exposure to vibration. In addition, ISO14837 [4] is focused on the emission-propagation-immission mechanisms of waves from the train-track system (source) to the building (receiver). It provides a guide on the measurement of experimental data, vibration evaluation and mitigation.

ISO14837 [4] also outlines suggested numerical modelling approaches. At the construction stage of a new railway line, comprehensive and detailed design models are recommended. These are typically computationally expensive, and include three-dimensional (3D) [5–9] models with full coupling between the train-track-soil-structure system. One alternative to 3D modelling is to use a two-and-a-half-dimensional (2.5D) approach [10–19]. These models assume the problem is continuous in the track direction and are not as such well suited for modelling transition zones, etc.

If the vibration assessment is to be undertaken at an earlier stage of railway line development, simplified scoping models [4] are often more useful. This is because they are faster running and often do not require as many input parameters.

Nelson and Sauernmann [20] presented such an empirical model to assess re-radiated ground-borne noise and vibration in buildings by combining line source response and force density. Field impact-testing procedures were used to evaluate line source transfer functions, while vehicle-track force density was indirectly obtained. Madshus et al. [21] developed a semi-empirical model to predict both expected values and confidence regions of building vibrations. To do so, a statistical analysis of recorded vibrations due to high-speed trains was undertaken. This model was focused on the low frequency vibrations of buildings founded in soft soil. Alternatively, Rossi and Nicolini [22] presented an analytical approach calibrated using railway field vibration measurements. This allowed for the quantification of train type, train speed, track properties and distance to the track, on the free-field vibrations induced by railway traffic. With et al. [23] proposed an empirical model to predict

*Corresponding author. Tel.: +34 954487293
Email address: pedrogalvin@us.es (P. Galvín)

train-induced ground vibrations considering wheel force, train speed and distance to the track. Also, empirical approaches to estimate soil and building vibrations due to a train passage [24, 25] have been proposed by the Federal Railroad Administration (FRA) and the Federal Transit Administration (FTA) of the US Department of Transportation. The simplifications considered in these procedures [24, 25] were verified by the numerical model presented in reference [26]. Later, Hussein et al. [27] proposed a sub-modelling method to couple a train-track-soil 3D model with a building, using a 2D frame made of beam elements. Kouroussis et al. [28] developed a decoupled approach, using only the finite element modelling, for characterizing building vibrations induced by adjacent tramway network with an important rail unevenness (local defect). Connolly et al. [29, 30] presented a scoping tool, called Scoperail, to instantly compute vibrations due to train passages. A machine learning approach to obtain free-field vibrations was developed by using numerical records for a wide range of train speeds and soil types. These soil vibrations were coupled with empirical factors in order to predict indoor noise in buildings and structural vibrations levels due to high speed trains. A hybrid model was described by Triepaischajonsak et al. [31], that combined a detailed vehicle-track model formulated in the time domain with a layered ground model operating in the frequency domain, based on the formulation outlined by Kausel et al. [32]. Then, forces acting on the ground were obtained from the train-track model and used in the ground model to calculate free-field vibrations. Kuo et al. [33] developed a hybrid model where the source and propagation mechanisms are decoupled. The model combined recorded data and numerical predictions considering the definitions proposed in references [24, 25]. Recently, Kouroussis et al. [34] developed a hybrid experimental-numerical model to predict vibrations from urban railway traffic. The level of vibration was calculated by combining the force density obtained from a numerical train-track model with the mobility function measured through an experimental approach.

Building upon this previous body of scoping model research, this paper presents a new scoping methodology to evaluate the free-field vibrations, aimed at aiding vibration assessments undertaken during the planning stages of a new railway line. It is able to model the effect of a large variety of input variables using minimal computational effort. To do so, track-soil interaction to define the vibration transmission is modelled by modulating the soil Green's function [32, 35, 36] with a correction factor obtained using a neural network (NN) approach. This allows for the coupled track-soil response to be simulated in only the time it takes to compute the soils Green's function. Then, free-field predictions are assessed by combining this track-soil model with train-track excitations. The proposed method allows for the estimation of the ground vibration descriptors presented in references [29, 30], but also the soil response in the time and frequency domains (with low computational effort).

This paper is organised as follows. First, the scoping model is presented. Next, an experimental and numerical validation of the scoping model is undertaken. A sensitivity analysis is then carried out to showcase the model and determine the effect of several key parameters on vibration propagation. Finally, the accuracy of using the average shear wave velocity of a layered soil as defined in Eurocode 8 [37] and denoted as V_{s30} is quantified.

2. Numerical modelling

To calculate the field response (Figure 1), the train-track-soil system was divided into two primary sub-models: a track-soil sub-model (step 2.1) and a train-track sub-model (step 2.2). To minimise the computational demand required to compute these sub-models, the following modelling strategies were used:

- To calculate the track-soil transfer function $\tilde{\mathbf{u}}_{\mathrm{ff}}$ (Figure 1, step 2.1) the soil Green's function $\tilde{\mathbf{u}}_{\mathrm{g}}$ is computed in the absence of track. Then, to approximate the response of a combined track-ground system, the Green's function is modulated using a correction factor, calculated via a neural network procedure.
- The train-track forces $\mathbf{g}$ are calculated using a simplified finite element (FEM) track model where the underlying soil is modelled using a spring-damper element that approximates the underlying soil response (Figure 1, step 2.2).

The free field response $\mathbf{u}_{\mathrm{s}}$ (Figure 1, step 2.3) is then computed using the formulation in the frequency-wavenumber domain presented by Lombaert et al. [10]. The train-track forces and the track-soil transfer function are described below.

2.1. Track-soil transfer function

Many vibration prediction models consider track-soil interaction using comprehensive methodologies. However, these require a high computational cost. In order to avoid this, the proposed model estimates the track-soil transfer function $\tilde{\mathbf{u}}_{\mathrm{ff}}(\mathbf{x}, k_y, \omega)$ (Figure 1 step 2.1) by combining the Green's functions $\tilde{\mathbf{u}}_{\mathrm{g}}(\mathbf{x}, k_y, \omega)$ [32] (Figure 1 step 2.1.2) for a homogeneous or layered soil with a correction factor $\tilde{A}_g$ obtained using a neural network (Figure 1 step 2.1.1). Note that the sub-indices ff and g indicate free-field response and Green's functions, respectively, and a tilde indicates a variable in the frequency-wavenumber domain. The track-soil transfer function $\tilde{\mathbf{u}}_{\mathrm{ff}}(\mathbf{x}, k_y, \omega)$ represents the response at a point $\mathbf{x} = \{d, y, 0\}$ located at the soil surface due to an impulsive vertical load at the rail. Correction factor $\tilde{A}_g$ depends on the track type and the soil properties. It is evaluated for a point $\mathbf{x}$ located at a distance d from the track centreline, a frequency ω and a wavenumber k_y. The track-soil transfer function at a point $\mathbf{x}$ can be obtained as:

$$\tilde{\mathbf{u}}_{\mathrm{ff}}(\mathbf{x}, k_y, \omega) = \tilde{A}_g(d, k_y, \omega)\tilde{\mathbf{u}}_{\mathrm{g}}(\mathbf{x}, k_y, \omega) \tag{1}$$

A NN approach to assess the correction factor $\tilde{A}_g(d, k_y, \omega)$ was selected because NN procedures are suitable methods to capture wave propagation models due to their ability for non-linear regression. NN approaches have been used to predict strong motion duration in earthquake engineering [38], to evaluate the effectiveness of trenches to reduce ground-borne vibration [39], to estimate fundamental period of vibration and maximum displacement of a building [40], to assess acceleration response spectra from tremors in the mining industry [41] and to detect damage on a railway bridge due to train passage [42].

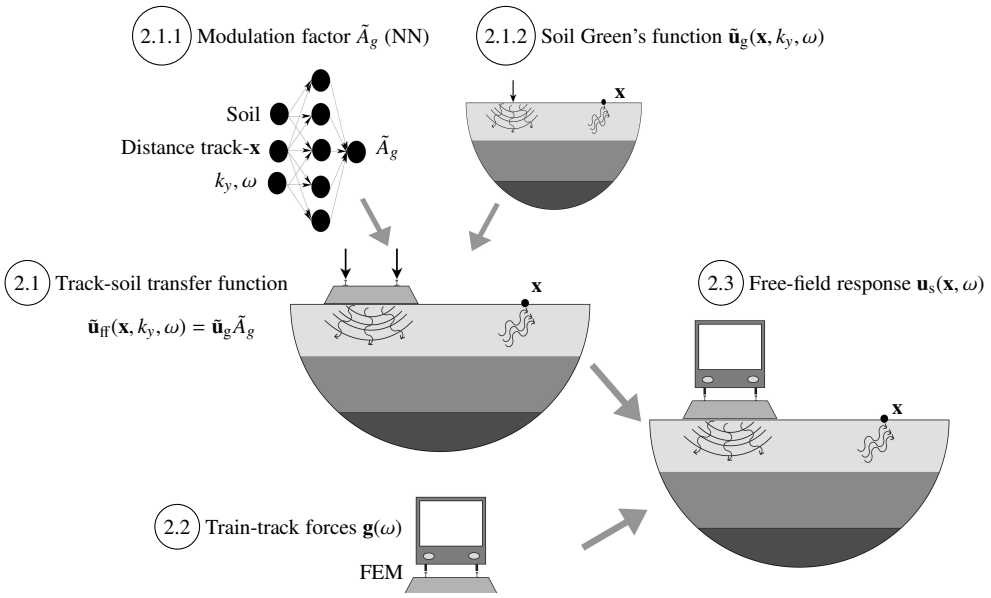

Figure 1: Scheme of the scoping model.

2.1.1. NN architecture

In order to estimate the correction factor $\tilde{A}_g$ (Equation (1)), a multilayer perceptron (MLP) neural network architecture with a back-propagation training algorithm [43] was chosen (Figure 2). One, two and three hidden layers were tested. A NN framework with four layers (one input, two hidden and one output) was chosen to construct the proposed model.

The correction factor $\tilde{A}_g$ modulates the Green's function $\tilde{\mathbf{u}}_g(\mathbf{x}, k_y, \omega)$ to evaluate the track-soil function $\tilde{\mathbf{u}}_{ff}(\mathbf{x}, k_y, \omega)$ at a point $\mathbf{x}$, a frequency ω and a wavenumber k_y. Coefficient $\tilde{A}_g$ depends on the track type and the soil properties. To build NN architecture ballasted and slab tracks were considered. Simplified soil profiles were used to build the NN model, using the average shear wave velocity V_{s30} as defined in Eurocode 8 [37], and computed as:

$$V_{s30} = \frac{30\ [\mathrm{m}]}{\sum_i^{N_s} \frac{h_i}{c_{s_i}}} \tag{2}$$

where h_i is the thickness of the $i-$th layer, N_s the total number of layers in the top 30 m and c_{s_i} the shear wave velocity of the $i-$th layer.

V_{s30} can be used to define a homogeneous soil, however it is non-unique because a variety of layered soils can be represented using the same value of V_{s30}. Therefore to further define the soil, the proposed model uses two additional variables: the depth h_1, and the shear wave velocity c_{s_1} of the upper layer. Then, the input layer (Figure 2) contains six inputs parameter: soil parameters c_{s_1}, h_1, V_{s30}, the distance d between the evaluated point $\mathbf{x}$ and the track, frequency ω and wavenumber. The wavenumber is represented by the non-dimensional wavenumber $k_{dy} = k_y c_{s_1}/\omega$. In the case of a homogeneous soil, the shear wave velocity of the upper layer matches with the V_{s30} parameter $c_{s_1} = V_{s30}$, with $h_1 = 30\,\mathrm{m}$.

In order to optimise the NN architecture, successive tests were developed modifying the number of neurons in the hidden layers. It was observed that 20 and 10 neurons in the first and second hidden layer, respectively, were optimal because performance did not improve when a larger number was used. The output layer has two parameters because the correction factor $\tilde{A}_g$ is a complex number. Therefore it is defined using its modulus $\left|\tilde{A}_g\right|$ and argument $arg\left(\tilde{A}_g\right)$:

$$\tilde{A}_g = \left|\tilde{A}_g\right| e^{\arg\left(\tilde{A}_g\right) i} \tag{3}$$

The objective of the NN procedure is to ensure the free-field

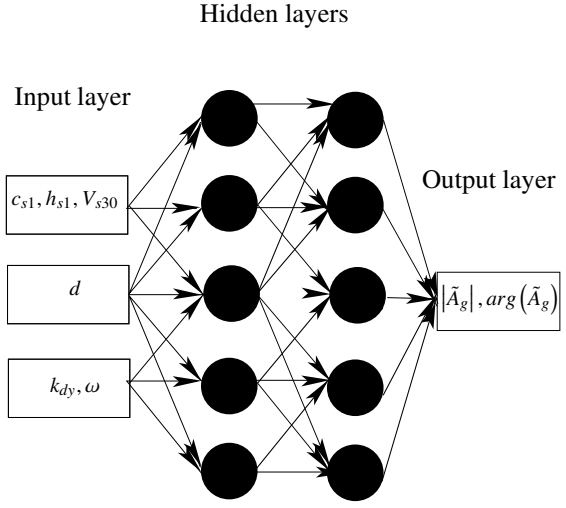

Figure 2: Neural network model schematic.

response of the modulated track-soil model is equal to the response of the true, coupled track-soil model, i.e.:

$$\tilde{\mathbf{u}}_{ff}^{p} = \tilde{\mathbf{u}}_{ff}^{r} \tag{4}$$

being $\tilde{\mathbf{u}}_{ff}^{p}$ and $\tilde{\mathbf{u}}_{ff}^{r}$ the track-soil transfer function obtained from the proposed model (super-index p) (Equation (1)) and com-

puted by using the reference model [14] (super-index r), respectively. Substituting Equations (3) and (4) into Equation (1) and considering the exponential forms of the track-soil transfer function $\tilde{\mathbf{u}}_{\mathrm{ff}}^{r}$ and the Green's functions $\tilde{\mathbf{u}}_{\mathrm{g}}$, the following expression can be obtained:

$$\left|\tilde{\mathbf{u}}_{\mathrm{ff}}^{r}\right| e^{\arg\left(\tilde{\mathbf{u}}_{\mathrm{ff}}^{r}\right)i} = \left|\tilde{A}_g\right| e^{\arg\left(\tilde{A}_g\right)i} \left|\tilde{\mathbf{u}}_{\mathrm{g}}\right| e^{\arg\left(\tilde{\mathbf{u}}_{\mathrm{g}}\right)i} \tag{5}$$

To obtain the reference values required to train the neural network, the modulus $\left|\tilde{A}_g\right|$ and argument $\arg\left(\tilde{A}_g\right)$ are obtained using Equation (5):

$$\left|\tilde{A}_g\right| = \frac{\left|\tilde{\mathbf{u}}_{\mathrm{ff}}^{r}\right|}{\left|\tilde{\mathbf{u}}_{\mathrm{g}}\right|} \tag{6}$$

$$\arg\left(\tilde{A}_g\right) = \arg\left(\tilde{\mathbf{u}}_{\mathrm{ff}}^{r}\right) - \arg\left(\tilde{\mathbf{u}}_{\mathrm{g}}\right) \tag{7}$$

The aim of the NN procedure is to map the weighted inputs (e.g. distance) to outputs (i.e. vibration). First, weighted inputs are assumed and the resulting predicted outputs are compared against the known outputs to quantify the error. This error is fed back through the network using a back-propagation training algorithm. The input weightings are then modified and the process is repeated until convergence.

The NN approach was developed by using the `Matlab Neural Network Toolbox` [44]. A tangent hyperbolic function was used as the activation function in the hidden layers due to its faster convergence compared to nonsymmetric functions [45]. The NN architecture was trained using the Levenberg-Marquardt algorithm that has been shown to be one of the fastest methods for training NNs [46]. Also, to evaluate the performance of the NN model and select the best framework, mean squared error (MSE) and coefficient of determination (R^2) were used, which are defined as follows:

$$MSE = \frac{1}{N_n}\sum_{i=1}^{N_n}\left(X_i - \hat{X}_i\right)^2 \tag{8}$$

$$R^2 = 1 - \frac{\sum_{i=1}^{N_n}\left(X_i - \hat{X}_i\right)^2}{\sum_{i=1}^{N_n}\left(X_i - \mathrm{mean}(X)\right)^2} \tag{9}$$

where X_i and $\hat{X}_i$ are the output targets and predicted outputs, respectively, and N_n is the size of the sample. These statistical indices allow the proposed model to be adjusted to approximate the reference model defined in Equation (4). When MSE and R^2 approach 0 and 1, respectively, accurate predictions of the track-soil function $\tilde{\mathbf{u}}_{\mathrm{ff}}^{r}$ are obtained [47–49].

To reduce the prediction error, tests were performed by transforming the raw input and output target data [50]:

- $\mathrm{Re}\left(\tilde{A}_g\right)$ and $\mathrm{Im}\left(\tilde{A}_g\right)$ parts were used as the output parameters.
- Modulus $\left|\tilde{A}_g\right|$ and argument $\arg\left(\tilde{A}_g\right)$ ("wrapped" and "unwrapped") were used as the output parameters.
- Input data were normalised to the interval $[-1, 1]$.
- Output target data were normalised to the interval $[-1, 1]$ and $[0, 1]$.
- Output target data modulus $\left|\tilde{A}_g\right|$ were transformed to logarithmic scale.

Unfortunately these modifications did not improve performance so were discarded. However, results were improved when output target data argument was wrapped to 2π rad and output target data modulus was presented as:

$$K_g = 20\log_{10}\left|\tilde{A}_g\right| \tag{10}$$

Then, Equations (7) and (10) were used to build the output targets.

2.1.1.1 NN database construction

A large number of data points are required to train and evaluate a NN. A discussion about this issue is done in Section 6. To do so, observation points were chosen at distances d from 10 to 50 m. Three types of soil were considered: soft, medium and stiff, corresponding to types D, C and B, as classified in Eurocode 8 [37] (Table 1). Rock type A was discarded because it is less commonly found in railway lines.

Table 1: Soil types based on Eurocode 8.

	Description	V_{s30} [m/s]
A	Rock outcrop	> 800
B	Very dense sand or gravel, or very stiff clay	360 – 800
C	Dense to medium-dense sand or gravel, or stiff clay	180 – 360
D	Loose-to-medium sand or gravel	< 180

A sample of 60 different layered soils was randomly generated considering the following parameters:

- Number of layers N was considered to be within the range $1 - 4$.
- To avoid locating the half-space at large depths where V_{s30} is not a good estimator of soil conditions [51], the sum of layer depths was considered to be below 30 m: $\sum_{i=1}^{N} h_i \leq 30$ m.
- In order to obtain layered soils properties compatible with (Table 1), the shear wave velocity of each layer was considered to be in the range $c_s = 100 - 800$ m/s.
- Layer stiffness increased with the depth.
- Density and Poisson's ratio were $\rho = 1800\,\mathrm{kg/m^3}$ and $\nu = 0.33$, for all layers.

Figure 3 shows the breakdown of the characteristics of the generated layered soils in the form of histograms. It can be observed that several soils presented an upper layer with depth below $h_1 = 10$ m and shear wave velocity around $c_{s_1} = 200$ m/s (Figures 3.(a) and 3.(b)). Also medium and stiff soils with V_{s30} values from 280 m/s to 500 m/s were mainly found in the sample of soils (Figure 3 (c)).

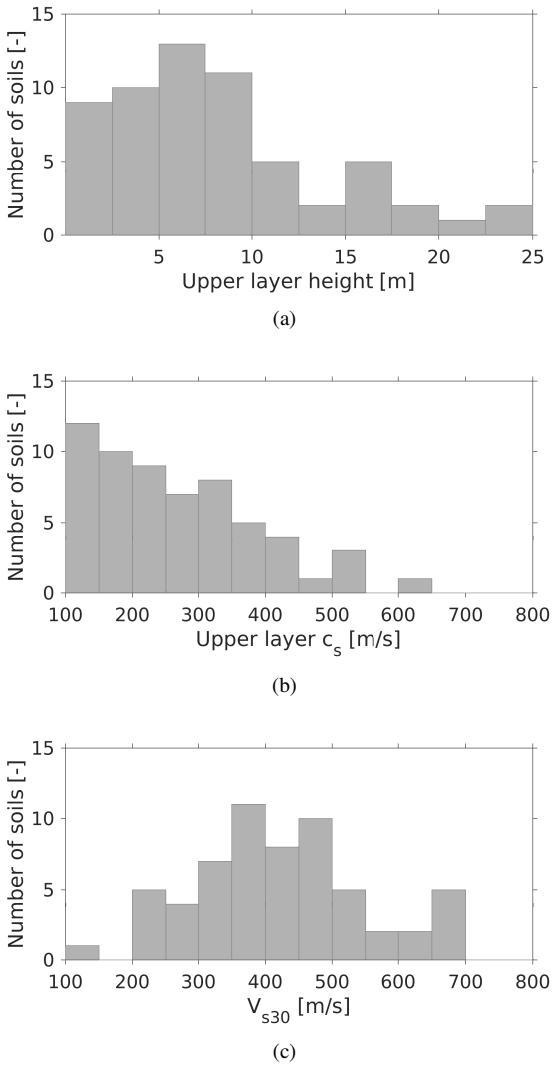

Figure 3: Histograms of sample of soils properties: (a) upper layer height, (b) upper layer shear wave velocity and (c) V_{s30}.

Another sample of 60 homogeneous soils was built upon this previous sample of layered soils considering shear wave velocity $c_s = V_{s30}$, where V_{s30} was obtained from the sample of layered soils. So, the database set was constructed from 120 soils.

The output targets (Equations (7) and (10)) were calculated using the Green's functions $\tilde{\mathbf{u}}_{\mathrm{g}}(\mathbf{x}, k_y, \omega)$ computed for the sample of layered and homogeneous soils. The reference model [14] used to obtain the track-soil transfer functions $\tilde{\mathbf{u}}^r_{\mathrm{ff}}(\mathbf{x}, k_y, \omega)$ considered ballasted and slab tracks situated on top of an embankment, supported by this sample of soils. Table 2 summarises the properties of the ballasted and slab tracks (Figures 5 and 6). The material properties of the embankment were chosen equal to those of the top layer of the soil. A linear hysteretic damping model was used for all constituents of the ballasted and slab track structure. The properties were obtained from published literature (among them [8]).

Output targets were obtained for the sample of 120 soils and considering distances $d : \{10, 20, 30, 40, 50\}$ m from the track centreline. The sample of 75 frequencies was within the range 0.5 Hz - 150 Hz. A sample of 98 non-dimensional wavenumber k_{dy} values from 0 to 100 was employed. This resulted in: 120 soil types × 5 distances × 75 frequencies × 98 wavenumbers = 4410000 data points. These output targets were divided in two subsamples: three-quarters for NN training and one-quarter for NN testing.

Table 2: Ballasted and slab track properties.

RAIL	
Bending stiffness $E_{\mathrm{r}} I_{\mathrm{r}}$ $\left[\mathrm{N/m^2}\right]$	6.18×10^6
Mass per unit length $\rho_{\mathrm{r}} A_{\mathrm{r}}$ [kg/m]	60.83
Loss factor η_{r}	0.05
RAIL PAD	
Equivalent stiffness $\overline{k}_{\mathrm{rp}}$ $\left[\mathrm{N/m^2}\right]$	150×10^6
Loss factor η_{rp}	0.25
SLEEPER	
Spacing d_{sl} [m]	0.60
Length l_{sl} [m]	2.60
Width b_{sl} [m]	0.35
Height h_{sl} [m]	0.22
Mass per sleeper m_{sl} [kg]	300
Rotational inertia $\rho_{\mathrm{sl}} \overline{I}_{\mathrm{sl}}$ $\left[\mathrm{kgm^2/m}\right]$	567
BALLAST	
Length at the top l_{b1} [m]	2.60
Length at the bottom l_{b2} [m]	2.87
Width b_{b} [m]	0.35
Height h_{b} [m]	0.3
Equivalent mass $\overline{m}_{\mathrm{b}}$ [kg/m]	796
Vertical stiffness k_{b} [N/m]	500×10^6
Loss factor η_{b}	1.0
SLAB	
Length l_{slab} [m]	2.60
Height h_{slab} [m]	0.30
Bending stiffness $E_{\mathrm{slab}} I_{\mathrm{slab}}$ $\left[\mathrm{Nm^2}\right]$	117×10^6
Mass per unit length $\rho_{\mathrm{slab}} A_{\mathrm{slab}}$ [kg/m]	1950
Loss factor η_{slab}	0.01
EMBANKMENT	
Length at the top l_{e1} [m]	3.50
Length at the soil surface l_{e2} [m]	7.00
Height h_{e} [m]	1.50

2.1.1.2 NN testing

Once the NN was trained and its architecture finalised, model performance was evaluated. Figure 4 shows a scatter plot to

evaluate the agreement in the predictions of the correction factor $\tilde{A}_g$. The indices R^2 and MSE are related in Table 3. It can be observed that the agreement in the estimation of the modulus parameter K_g is quite good (Figure 4.(a)). Regarding the argument parameter $arg\left(\tilde{A}_g\right)$, the agreement is not quite as strong (Figure 4.(b)). However, as shown in the next section, the NN predictions of the correction factor $\tilde{A}_g$ provide a reasonable estimate of the track-soil transfer function $\tilde{\mathbf{u}}_{\mathrm{ff}}$.

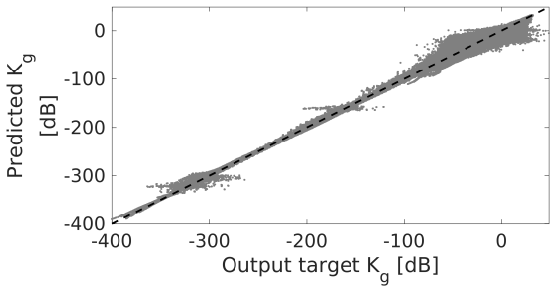

(a)

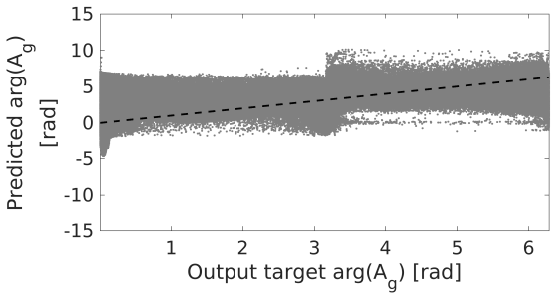

(b)

Figure 4: Results of neural network model of the (a) K_g and (b) $arg\left(\tilde{A}_g\right)$ parameters.

Table 3: NN performance.

		Training set		Testing set	
		R^2	MSE	R^2	MSE
Ballasted track	K_g	0.99	3.7 dB^2	0.99	3.7 dB^2
	$arg\left(\tilde{A}_g\right)$	0.64	1.2 rad^2	0.64	1.2 rad^2
Slab track	K_g	0.99	5.9 dB^2	0.99	5.9 dB^2
	$arg\left(\tilde{A}_g\right)$	0.75	1.6 rad^2	0.75	1.6 rad^2

2.2. Track-soil forces

2.2.1. Track model

The track-soil forces (Figure 1 step 2.2) are calculated using a simplified 2.5D FEM model (Figures 5 and 6). The model allows both linear hysteretic or viscous damping models for the constituents in the ballasted and slab track structure.

For the ballasted track model, the rails are represented using Euler-Bernoulli beams with a bending stiffness $E_{\mathrm{r}}I_{\mathrm{r}}$ and a mass $\rho_{\mathrm{r}}A_{\mathrm{r}}$ per unit length. The rail displacements are denoted as $u_{\mathrm{r}1}(x_1, t)$ and $u_{\mathrm{r}2}(x_2, t)$. The position of the rails is determined by x_1 and x_2, with $x_2 - x_1$ equal to the track gauge w_{r}. The internal energy dissipation in the rail is modelled using a loss factor η_{r}.

The rail pads are modelled as continuous spring-damper connections. The rail pad stiffness k_{rp} and damping coefficient c_{rp} of a single rail pad are used to calculate the equivalent stiffness $\overline{k}_{\mathrm{rp}} = k_{\mathrm{rp}}/d_{\mathrm{sl}}$ and damping $\overline{c}_{\mathrm{rp}} = c_{\mathrm{rp}}/d_{\mathrm{sl}}$ where d_{sl} is the sleeper spacing. Alternatively, a loss factor η_{rp} can be used to describe rail pad behaviour as, $\overline{k}_{\mathrm{rp}} = \overline{k}_{\mathrm{rp}}(1 + i\eta_{\mathrm{rp}})$.

The concrete sleepers are assumed to be rigid in the plane of the track cross section, so that the vertical sleeper displacements along the track are determined by the vertical displacement $u_{\mathrm{sl}}(x, t)$ and rotation $\theta_{\mathrm{sl}}(x, t)$ at the centre of gravity of the sleeper. The sleepers are modelled as a uniformly distributed mass $\overline{m}_{\mathrm{sl}} = m_{\mathrm{sl}}/d_{\mathrm{sl}}$. The rotational inertia of the sleeper is estimated as $\rho_{\mathrm{sl}}\overline{I}_{\mathrm{sl}} = \rho_{\mathrm{sl}}I_{\mathrm{sl}}/d_{\mathrm{sl}}$.

The ballast bed is modelled using a set of distributed linear springs and dampers. The smeared ballast stiffness $\overline{k}_{\mathrm{b}}$ is computed from the vertical spring stiffness k_{b} per sleeper as $k_{\mathrm{b}}/d_{\mathrm{sl}}$. The viscous damping in the ballast bed is accounted for by a ballast impedance and equals $\overline{k}_{\mathrm{b}} + i\omega\overline{c}_{\mathrm{b}}$. Alternatively, a loss factor η_{b} can be used to describe ballast behaviour as $\overline{k}_{\mathrm{b}} = \overline{k}_{\mathrm{b}}(1 + i\eta_{\mathrm{b}})$. The equivalent ballast mass $\overline{m}_{\mathrm{b}}$ is computed using the ballast mass m_{b} under each sleeper as $m_{\mathrm{b}}/d_{\mathrm{sl}}$. The ballast mass m_{b} is estimated from the height h_{b} of the ballast layer and lengths $l_{\mathrm{b}1} = l_{\mathrm{sl}}$ and $l_{\mathrm{b}2}$ at the top and the bottom of the ballast layer, respectively, as $m_{\mathrm{b}} = 0.5\rho_{\mathrm{b}}h_{\mathrm{b}}(l_{\mathrm{b}1} + l_{\mathrm{b}2})b_{\mathrm{sl}}$.

The embankment is represented using an Euler-Bernoulli beam with a bending stiffness $E_{\mathrm{e}}I_{\mathrm{e}}$, a torsional rigidity $G_{\mathrm{e}}J_{\mathrm{e}}$, a loss factor η_{e}, a rotational inertia $\rho_{\mathrm{e}}I_{pe}$, and a mass $\rho_{\mathrm{e}}A_{\mathrm{e}}$ per unit length. The embankment properties are approximated to be equal to the uppermost soil layer. The effect of the embankment on ground vibrations due to railway traffic has been previously studied by other authors (among them [14, 52]).

A ballast mat can be simulated using spring-damper elements between the embankment and the ballast with equivalent stiffness and damping (or loss factor) $\overline{k}_{\mathrm{m}}$ and $\overline{c}_{\mathrm{m}}$ (or η_{m}), respectively.

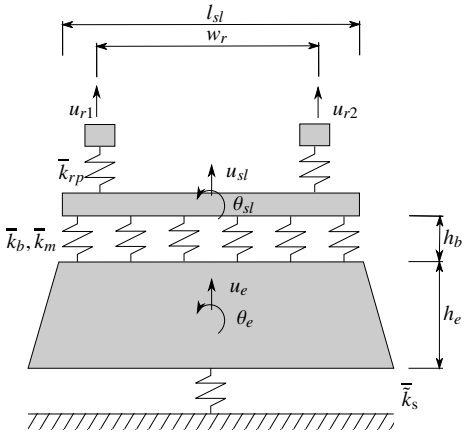

Figure 5: Cross section of ballasted track model.

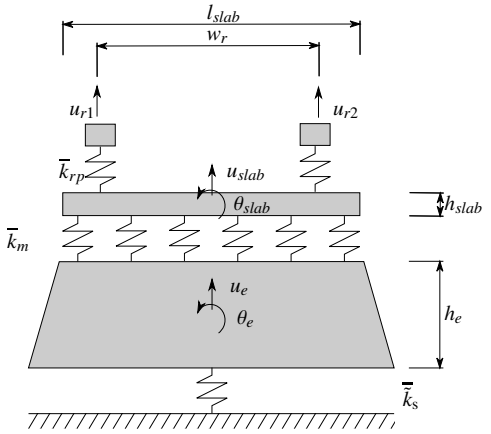

Figure 6: Cross section of slab track model.

For the slab track model, the rails, rail pads and embankment are modelled as in the ballasted track model. The slab is represented by an Euler-Bernoulli beam with a bending stiffness $E_{\text{slab}}I_{\text{slab}}$, a torsional rigidity $G_{\text{slab}}J_{\text{slab}}$, a rotational inertia $\rho_{\text{slab}}I_{p\text{slab}}$, a loss factor η_{slab} and a mass per unit length $\rho_{\text{slab}}A_{\text{slab}}$. A floating slab track can be represented as in the case of the ballast mat.

The underlying soil is represented using a spring-damper element with stiffness $\overline{\tilde{k}}_s(k_y, \omega)$. The equivalent stiffness and damping of the soil is estimated by the vertical soil response computed from the Green's function for a homogeneous or layered half-space. The soil flexibility $1/\overline{\tilde{k}}_s(k_y, \omega)$ is obtained from the soil response induced by a unit vertical load applied at the soil surface and evaluated at a point located at a distance $d = w_r/2$ from the track centerline (under the rail). Note that because the spring-damper element does not consider the effect of a moving load, the model ignores the dynamic effects that may be induced when approaching critical velocity [53]. The continuity of displacement is fulfilled between the soil and the track.

2.2.1.1 2.5D FEM formulation

The 2.5D FEM formulation follows that outlined in [14]:

$$\begin{aligned}&\left[-\omega^2\mathbf{M}_{\text{bb}} + \mathbf{K}^0_{\text{bb}} - ik_y\mathbf{K}^1_{\text{bb}} - k_y^2\mathbf{K}^2_{\text{bb}} + ik_y^3\mathbf{K}^3_{\text{bb}} + k_y^4\mathbf{K}^4_{\text{bb}}\right.\\ &\left.+\tilde{\mathbf{K}}^{\text{s}}_{\text{bb}}(k_y, \omega)\right]\tilde{\mathbf{u}}_{\text{b}}(k_y, \omega) = \tilde{\mathbf{f}}_{\text{b}}(k_y, \omega)\end{aligned} \tag{11}$$

where $\mathbf{K}^0_{\text{bb}}$, $\mathbf{K}^1_{\text{bb}}$, $\mathbf{K}^2_{\text{bb}}$, $\mathbf{K}^3_{\text{bb}}$ and $\mathbf{K}^4_{\text{bb}}$ are the stiffness matrices, $\mathbf{M}_{\text{bb}}$ is the mass matrix, $\tilde{\mathbf{f}}_{\text{b}}(k_y, \omega)$ is the external load vector, and $\mathbf{K}^{\text{s}}_{\text{bb}}(k_y, \omega)$ represents the dynamic soil stiffness matrix. For simplicity, matrices $\mathbf{K}^1_{\text{bb}}$, $\mathbf{K}^2_{\text{bb}}$ and $\mathbf{K}^3_{\text{bb}}$ are discarded so that the proposed model does not contain any volume or shell elements. The finite element matrices $\mathbf{M}_{\text{bb}}$, $\mathbf{K}^0_{\text{bb}}$ and $\mathbf{K}^4_{\text{bb}}$ in Equation (11) are independent of wavenumber k_y and frequency ω, and are only assembled once. Equation (11) is now further elaborated by dividing the finite element degrees of freedom $\tilde{\mathbf{u}}_{\text{b}}(k_y, \omega)$ into internal degrees of freedom $\tilde{\mathbf{u}}_{\text{b}_1}(k_y, \omega)$ and degrees of freedom $\tilde{\mathbf{u}}_{\text{b}_2}(k_y, \omega)$ on the soil-structure interface:

$$\begin{aligned}&\left(-\omega^2\begin{bmatrix}\mathbf{M}_{\text{b}_1\text{b}_1} & \mathbf{M}_{\text{b}_1\text{b}_2}\\ \mathbf{M}_{\text{b}_2\text{b}_1} & \mathbf{M}_{\text{b}_2\text{b}_2}\end{bmatrix} + \begin{bmatrix}\mathbf{K}^0_{\text{b}_1\text{b}_1} & \mathbf{K}^0_{\text{b}_1\text{b}_2}\\ \mathbf{K}^0_{\text{b}_2\text{b}_1} & \mathbf{K}^0_{\text{b}_2\text{b}_2}\end{bmatrix} + k_y^4\begin{bmatrix}\mathbf{K}^4_{\text{b}_1\text{b}_1} & \mathbf{K}^4_{\text{b}_1\text{b}_2}\\ \mathbf{K}^4_{\text{b}_2\text{b}_1} & \mathbf{K}^4_{\text{b}_2\text{b}_2}\end{bmatrix} +\right.\\ &\left.\begin{bmatrix}0 & 0\\ 0 & \tilde{\mathbf{K}}^{\text{s}}_{\text{b}_2\text{b}_2}(k_y, \omega)\end{bmatrix}\right)\begin{bmatrix}\tilde{\mathbf{u}}_{\text{b}_1}(k_y, \omega)\\ \tilde{\mathbf{u}}_{\text{b}_2}(k_y, \omega)\end{bmatrix} = \begin{bmatrix}\tilde{\mathbf{f}}_{\text{b}_1}(k_y, \omega)\\ \tilde{\mathbf{f}}_{\text{b}_2}(k_y, \omega)\end{bmatrix}\end{aligned} \tag{12}$$

The dynamic soil stiffness matrix $\tilde{\mathbf{K}}^{\text{s}}_{\text{b}_2\text{b}_2}(k_y, \omega) = \overline{\tilde{k}}_s(k_y, \omega)$ is computed by means of the Green's function [32] (Figure 1 step 2.1.2).

The following describes the evaluation of train-track interaction forces (Figure 1 step 2.2). Both quasi-static excitation and dynamic excitation due to random track unevenness are taken into account [54], and the dynamic contributions depend upon the rail displacements $\tilde{\mathbf{u}}_{\text{r}}(k_y, \omega)$ obtained using Equation (12).

2.2.2. Vehicle loading

Firstly, a power spectral density (PSD) function is assumed for the random track unevenness:

$$\tilde{S}_{\text{rzz}}(k_y) = \tilde{S}_{\text{rzz}}(k_{y0})\left(\frac{k_y}{k_{y0}}\right)^{-w} \tag{13}$$

where $\tilde{S}_{\text{rzz}}(k_{y0})$ is the reference value of the PSD at k_{y0} and w is the exponent that determines how strong the PSD function decreases with increasing wavenumber k_y. The coefficients $\tilde{S}_{\text{rzz}}(k_{y0})$ and w are obtained from standards [55]. $w = 3.5$ and $k_{y0} = 1\,\text{rad/m}$ are commonly assumed for railway unevenness. The value of $\tilde{S}_{\text{rzz}}(k_{y0})$ depends on the track maintenance [56]: $5 \times 10^{-7}\,\text{m}^3$ (poor), $1.25 \times 10^{-7}\,\text{m}^3$ (medium) and $1 \times 10^{-9}\,\text{m}^3$ (good).

The rail unevenness $\mathbf{u}_{\text{w/r}}(\omega)$ is evaluated as:

$$\mathbf{u}_{\text{w/r}}(\omega) = \mathbf{T}(\omega)\frac{1}{v}\tilde{u}_{rz}\left(-\frac{\omega}{v}\right) \tag{14}$$

where $\tilde{u}_{rz}(k_y)$ is the wavenumber transform of the rail unevenness $u_{rz}(y)$ and $\mathbf{T}(\omega)$ is a vector that collects the phase shift for each axle moving at a constant speed v, being:

$$u_{rz}(y) = \sum_{m=1}^{n}\sqrt{2\tilde{S}_{rzz}(k_{ym})\Delta k_y}\cos(k_{ym}y - \theta_m) \tag{15}$$

where $k_{ym} = m\Delta k_y$ is the wavenumber sampling, Δk_y the wavenumber bin and θ_m represents random phase angles uniformly distributed in the interval $[0, 2\pi]$. The dynamic forces $\mathbf{g}_d(\omega)$ are computed from the track and vehicle compliances assuming a perfect contact between both [10]:

$$\mathbf{u}_{\text{c}}(\omega) = \mathbf{u}_{\text{r}}(\omega) + \mathbf{u}_{\text{w/r}}(\omega) \tag{16}$$

where $\mathbf{u}_{\text{c}}$ represents the displacements at the vehicle-track interface and, both the rail displacements $\mathbf{u}_{\text{r}}(\omega)$ and the rail unevenness $\mathbf{u}_{\text{w/r}}(\omega)$ are evaluated at a fixed position in the moving frame of reference. The dynamic loads are computed as:

$$\left[\mathbf{C}^t(\omega) + \mathbf{C}^v(\omega)\right]\mathbf{g}_d(\omega) = -\mathbf{u}_{\text{w/r}}(\omega) \tag{17}$$

where $\mathbf{C}^v(\omega)$ is the vehicle compliance and $\mathbf{C}^t(\omega)$ is the track compliance.

The vehicle's unsprung mass is the train mass that influences mainly vertical dynamic loads [11], meaning vehicle compliance can be assessed as $\mathbf{C}^v(\omega) = \text{diag}(-1/(M_u\omega^2))$, where M_u is the unsprung axle mass.

Additionally, the track compliance C^t_{lk} relates the track displacement at the position of axle k due to a unit load at axle l. The track compliance is obtained from the rail impulse response $\tilde{u}_\text{r}$ using the following equation [10]:

$$\mathbf{C}^t_{lk}(\tilde{\omega}) = \frac{1}{2\pi}\int_{-\infty}^{+\infty} \tilde{u}_\text{r}(k_y, \tilde{\omega} + k_y v) e^{-\text{i}k_y(y_l - y_k)} \text{d}k_y \qquad (18)$$

where y_l and y_k are the positions of l-th and k-th axles respectively. Also, $\tilde{\omega} = \omega - k_y v$ and v is the train speed.

The quasi-static load of the k-th axle is determined by the weight w_k carried by the axle [10]:

$$g_{q_k}(\tilde{\omega}) = w_k 2\pi\delta(\tilde{\omega}) \qquad (19)$$

2.3. Free-field response

Once the track-soil transfer function $\tilde{\mathbf{u}}_\text{ff}$ (Equation (1)), the dynamic excitation $\mathbf{g}_d$ (Equation (17)) and the quasi-static excitation $\mathbf{g}_q$ (Equation (19)) are obtained, the soil response $\mathbf{u}_\text{s}(\mathbf{x}, \omega)$ due a train passage at speed v is determined by following the 2.5D formulation in the wavenumber-frequency domain described in reference [10]. The free-field response $\mathbf{u}_\text{s}(\mathbf{x}, \omega)$ is decomposed into its static $\mathbf{u}_\text{qs}$ and dynamic $\mathbf{u}_\text{ds}$ components $\mathbf{u}_\text{s}(\mathbf{x}, \omega) = \mathbf{u}_\text{qs}(\mathbf{x}, \omega) + \mathbf{u}_\text{ds}(\mathbf{x}, \omega)$. The static and dynamic contributions, u_qsi and u_dsi, in the i-th direction at a point $\mathbf{x}$ can be evaluated as:

$$u_\text{qsi}(\mathbf{x}, \omega) = \sum_{k=1}^{n_a} w_k \tilde{h}_\text{ffi}(y - y_k, \omega, 0) \qquad (20)$$

$$u_\text{dsi}(\mathbf{x}, \omega) = \frac{1}{2\pi}\sum_{k=1}^{n_a}\int_{-\infty}^{+\infty} \tilde{h}_\text{ffi}(y - y_k, \omega, \tilde{\omega}) g_{\text{d}_k}(\tilde{\omega}) \text{d}\tilde{\omega} \qquad (21)$$

where n_a is the number of axles and w_k, y_k and g_{d_k} refer to weight carried, position and dynamic load of the k-th axle respectively. A change of variables $\tilde{\omega} = \omega - k_y v$ is again considered and the relation $\tilde{h}_\text{ffi}(y - y_k, \omega, \tilde{\omega}) = \frac{1}{v}\tilde{u}_\text{ffi}(\mathbf{x}, \frac{\omega - \tilde{\omega}}{v}, \omega) \exp\left[-i\frac{\omega - \tilde{\omega}}{v}(y - y_k)\right]$ is used to express Equations (20) and (21) in compact forms.

2.4. Building response

After obtaining the free-field response, it can be used to compute the vibration within buildings located close to the line. To do so, the free-field response can be used as an input for a soil-structure interaction model such as [57]. This entire train-track-soil-building model has been combined into a `MATLAB` toolbox, however this present work focuses on the calculation of free-field vibration.

3. Experimental and numerical validation

In this section an experimental (i.e. field testing) and numerical validation of the proposed scoping model is undertaken.

3.1. Experimental validation

A field experiment was undertaken on the high-speed train (HST) line between Brussels and Köln. Accelerometers were used to record rail and sleeper receptances, free-field mobility and also the free-field vibrations generated during the passage of Thalys HST at a speed of $v = 294$ km/h. Table 6 shows the carriage length L_t, the distance between bogies L_b, the axle distance L_a, the total axle mass M_t and the unsprung axle mass M_u for all carriages. A ballasted track with the properties shown in Table 4 and supported by a layered subgrade with the characteristics shown in Table 5 was studied. A detailed description of the field work campaign is give in [10]. To validate the scoping model against the field data, both track response and free-field response were analysed.

Table 4: HST track Brussels-Köln.

RAIL	
Bending stiffness $E_\text{r}I_\text{r}$ $\left[\text{N/m}^2\right]$	6.45×10^6
Mass per unit length $\rho_\text{r}A_\text{r}$ [kg/m]	60.3
RAIL PAD	
Stiffness k_rp [N/m]	153.4×10^6
Damping c_rp [Ns/m]	13.5×10^3
SLEEPER	
Spacing d_sl [m]	0.6
Length l_sl [m]	2.5
Width b_sl [m]	0.235
Height h_sl [m]	0.205
Mass per sleeper m_sl [kg]	300
BALLAST	
Height h_b [m]	0.35
Equivalent mass $\overline{m}_\text{b}$ [kg/m]	582.6
Vertical stiffness k_b [N/m]	920.7×10^6
Damping c_b [Ns/m]	16.6×10^3

Table 5: Soil characteristics.

	h [m]	c_p [m/s]	c_s [m/s]	ξ [-]	ρ $\left[\text{kg/m}^3\right]$	ν
Layer 1	3	300	150	0.03	2000	0.333
Half-space	∞	560	280	0.03	2000	0.333

A track unevenness profile (Equation (13)) with reference value $\tilde{S}_{\text{r}zz}(k_{y0}) = 1.36 \times 10^{-8}\,\text{m}^3$ of the PSD at $k_{y0} = 1\,\text{rad/m}$ and an exponent $w = 3.5$ was considered. A more detailed experimental description is found in the original work [10].

Table 6: Geometrical and mass characteristics of the Thalys HST.

	No.of carriages	No.of axles	L_t[m]	L_b[m]	L_a[m]	M_t[kg]	M_u[kg]
Traction cars	2	4	22.15	14.00	3.00	17000	2027
End carriages	2	3	21.84	18.70	3.00	17000	2027
Central carriages	6	2	18.70	18.70	3.00	17000	2027

3.1.1. Track-soil system

Figure 7 shows a comparison between rail receptances calculated using the scoping model and those measured experimentally. The results presented in reference [10] are also presented. It is seen that the scoping model slightly overestimates experimental rail receptance up to 27 Hz. On the other hand, the curves from the scoping model are under the experimental response at mid and high frequencies. The agreement with the experimental result is less good than in those presented in reference [10], however this is expected due to the underlying simplifications and considered acceptable for a scoping model. A difference between both models of -22 dB at 100 Hz was found. In addition to the rail displacement $\tilde{\mathbf{u}}_\mathrm{r}$ the model can also compute sleeper receptance, as shown in Figures 7.(c) and 7.(d). A similar accuracy is found.

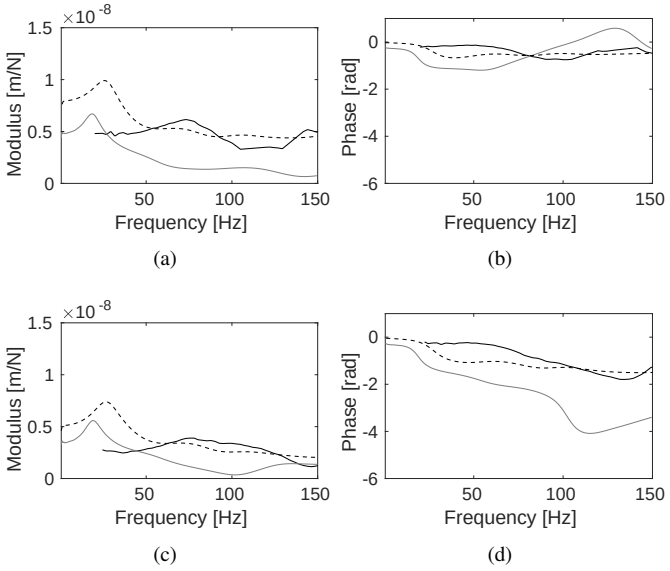

Figure 7: (Black line) experimental and (grey line) computed with the scoping model (a, b) rail and (c, d) sleeper receptances. Superimposed (dashed black line) the solution presented in reference [10].

Figure 8 shows experimental and computed mobilities of the track-soil system at distances $\{8, 16, 24, 32, 48, 64\}$ m from the track centreline. The free-field mobility predictions are overestimated, but the agreement is good and the computed results exhibit a similar frequency dependence compared to the experimental data. Differences between the scoping model and reference [10] increase with the frequency up to a value of -15 dB. The discrepancies at short distances from the track (Figures 8.(a) and 8.(b)) are because the NN approach was trained for a ballasted track over an embankment, while the HST line between Brussels and Köln is an at-grade track. The effect of the embankment is significant at the locations closer to the track [14, 52].

Figure 8 shows the effect of a $\pm 10\%$ variation in $|\tilde{A}_g|$-values, on the predicted vibration from the scoping model. The predictions are not highly affected by small changes in $|\tilde{A}_g|$-values and they present a consistent behaviour.

3.1.2. Free-field response

The one-third octave band center frequencies of the free-field response at distances $\{8, 16, 24, 32, 48, 64\}$ m from the track centreline due to a Thalys HST passage at $v = 294$ km/h are presented in Figure 9. The response from [10] is superimposed. The one-third octave band spectrum has been computed according to the German standard DIN 45672-2 [58] for a reference period T2 during which the response is considered to be stationary. The frequency content is concentrated at frequencies below 100 Hz, for both the scoping model and experimental results. In general, the computed response from the scoping model underestimates the experimental results. The discrepancies between both results computed using the scoping model and presented in [10] are in accordance with Figure 8.

Figure 10 shows the time history of the free-field response due to a Thalys passage at $v = 294$ km/h. The time domain response was evaluated from an inverse Fourier transform of the frequency response in the range from 0.5 to 150 Hz, with a frequency sampling of $\Delta f = 0.01$ Hz. The duration of both experimental and computed responses are increasing with the distance from the track. The accuracy to predict the amplitude of the free-field response due to a train passage is sufficient for the purpose of a preliminary study.

In accordance with the comparison shown in this section, it can be concluded that the scoping model presents a good agreement with the experimental results.

3.2. Numerical validation

To further validate the scoping model, its predictions were compared against a more comprehensive, 'reference' model. The reference model (Figure 11) is based upon a 2.5D boundary element-finite element methodology in the frequency-wavenumber domain [10, 14]. It was designed to compute the generation of railway vibrations and their propagation through the neighbouring soil. First, the track-soil transfer function $\tilde{\mathbf{u}}_\mathrm{ff}$ is calculated by modelling the track using FEM and the soil using the boundary element method (BEM). This result corresponds to the soil response due to an impulse load applied on the rails (Figure 11 step 2.1). Next, the train-track forces $\mathbf{g}(\omega)$ are calculated considering both quasi-static and dynamic contributions (Figure 11 step 2.2). Finally, the train-track interaction forces are combined with the track-soil transfer function, resulting in the free-field response due to train passage $\mathbf{u}_\mathrm{s}$ at a point $\mathbf{x}$ (Figure 11, step 2.3).

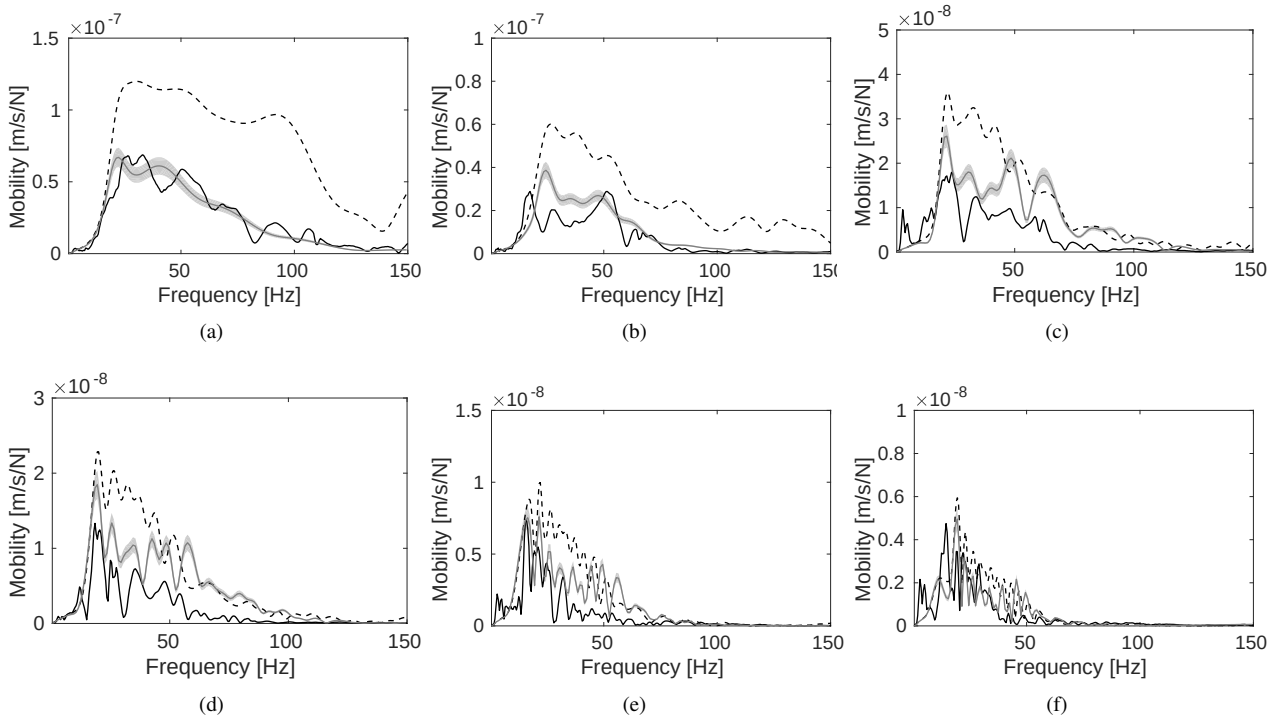

Figure 8: (Black line) the experimental and (grey line) computed with the scoping model free-field vertical mobility at a distance of: (a) 8 m; (b) 16 m; (c) 24 m; (d) 32 m; (e) 48 m and (f) 64 m from the track centerline. The effect of a ±10% variation in $|\tilde{A}_g|$-values is represented by the grey area. Superimposed (dashed black line) the solution presented in reference [10].

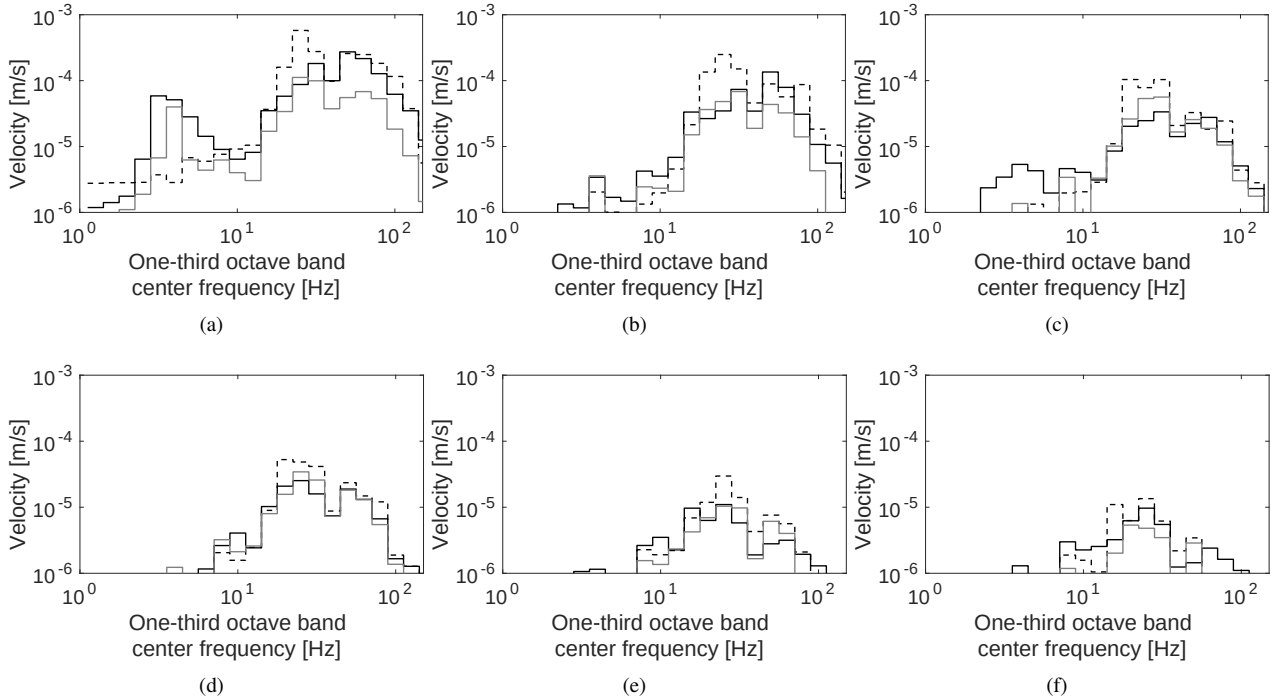

Figure 9: (Black line) the experimental and (grey line) computed with the scoping model one-third octave band center frequency of the vertical velocity at the free field at a distance of: (a) 8 m; (b) 16 m; (c) 24 m; (d) 32 m; (e) 48 m and (f) 64 m from the track centerline during the passage of the Thalys HST at a speed v = 294 km/h. Superimposed (dashed black line) the solution presented in reference [10]

.

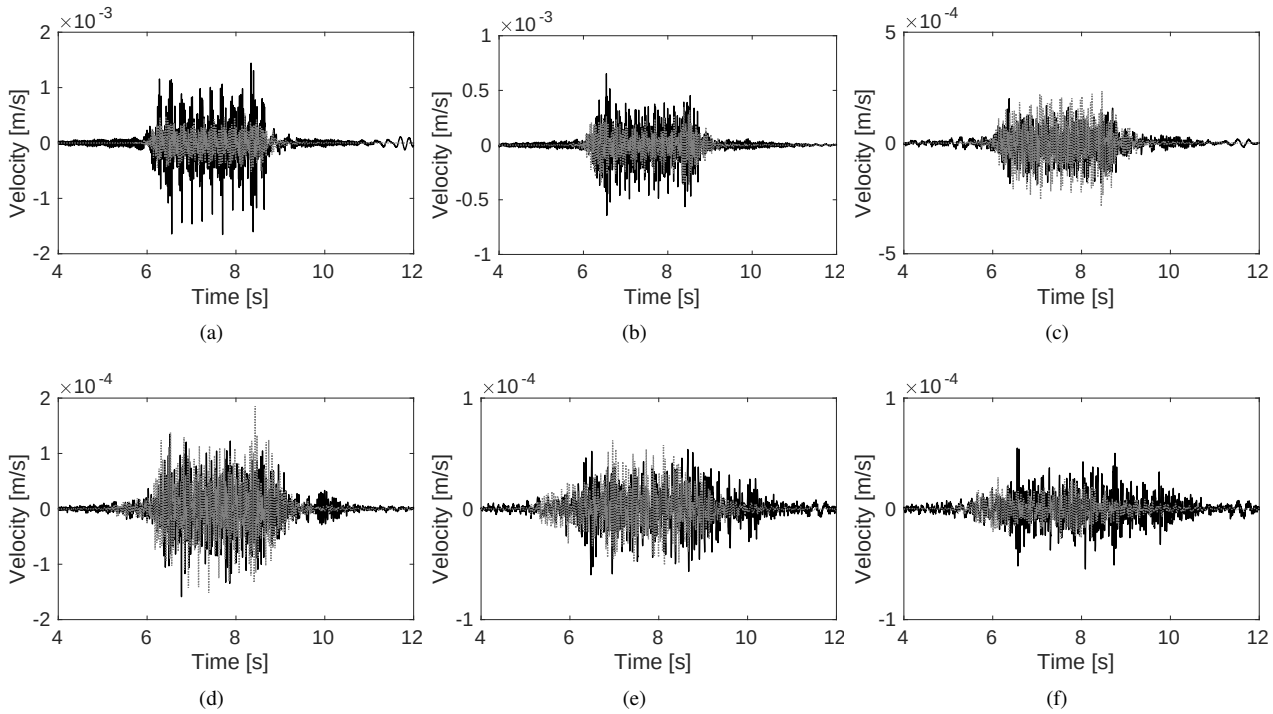

Figure 10: (Black line) the experimental and (grey line) computed with the scoping model time history of the vertical velocity at the free field at a distance of: (a) 8 m; (b) 16 m; (c) 24 m; (d) 32 m; (e) 48 m and (f) 64 m from the track centerline during the passage of the Thalys HST at a speed $v = 294$ km/h.

The scoping model has two main novelties: the use of a simplified 2.5D FEM track model, and a NN procedure to convert the soil Green's functions to the track-soil response. Therefore, a series of tests were performed to assess the accuracy of each new sub-model. To do so, a variety of modelling scenarios were analysed. Three track cases (ballasted track over an embankment, an at-grade ballasted track and a slab track over an embankment), four soil types and a train speed $v = 100$ km/h were considered. Quasi-static excitation and dynamic excitation due to random track unevenness were taken into account [11], and the same track unevenness profile was considered for all cases. The free-field mobility and free-field response due to railway traffic were obtained at a point located at a distance of $d = 20$ m from the track centreline.

Regarding the vehicle, a S-100 series train (Table 7) was simulated. It should be noted that because the train speed is below the critical velocity of the track system [59], the dynamic contribution will be dominant in the free-field response [11].

3.2.1. Train-track forces

To thoroughly validate the train-track forces sub-model, three track types were analysed. Track 1 was a classical ballasted track (Section 2.1.1 (Table 2)) supported by an embankment with identical mechanical properties as the underlying soil. Track 2 was a slab track (Figure 6) with identical rails, rail pads and embankment as Track 1 (Section 2.1.1 (Table 2)). Track 3 was identical to Track 1, however at-grade (i.e. without an embankment).

The soil was modelled as a homogeneous elastic half-space

Table 7: Geometrical and mass characteristics of the S-100 train.

	No.of carriages	No.of axles	L_t[m]	L_b[m]	L_a[m]	M_t[kg]	M_u[kg]
Traction cars	2	4	22.15	14.00	3.00	17185	2048
End carriages	2	3	21.84	18.70	3.00	11523	2003
Central carriages	6	2	18.70	18.70	3.00	15523	2003

with a shear wave velocity $c_s = 200$ m/s, a dilatational wave velocity $c_p = 400$ m/s and density $\rho = 1800$ kg/m^3. The material damping ratio ξ ($\eta/2 = \xi$) for both deviatoric and volumetric deformation had a value of 0.05.

Figure 12 shows rail receptances for the three type of tracks. It is seen that the low frequency response is slightly overestimated, but the agreement improves with increasing frequency. This is due to the dominant influence of track-soil interaction, in which the reference and scoping models differ. The reference method rigorously models the soil using BEM, while the scoping model uses a simplified methodology with a linear spring-damper to significantly reduce computational time.

Free-field mobilities for the three tracks are presented in Figure 13. It is seen that the shape and magnitude of response of both models match well. The ballasted track models overestimate the response up to 50 Hz (Figures 13.(a) and 13.(c)),

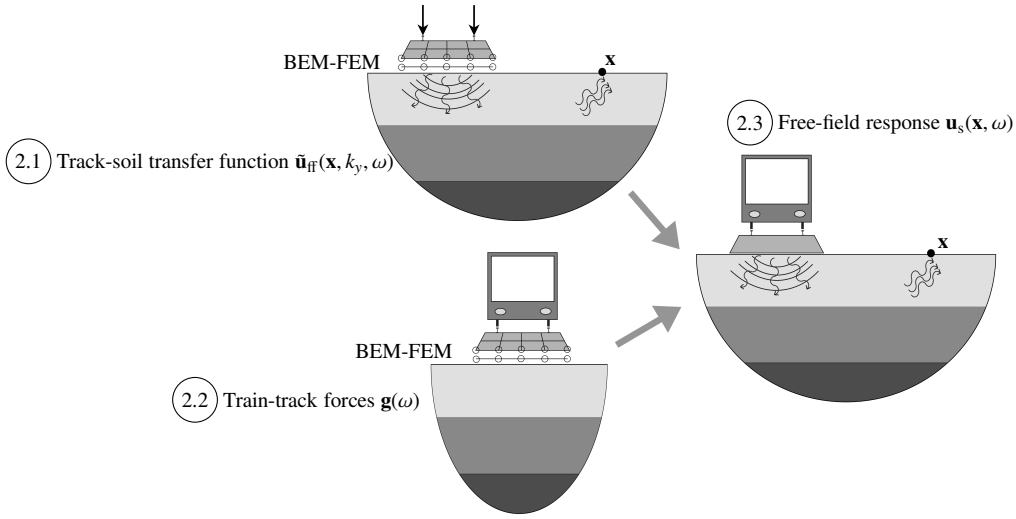

Figure 11: Scheme of the reference model.

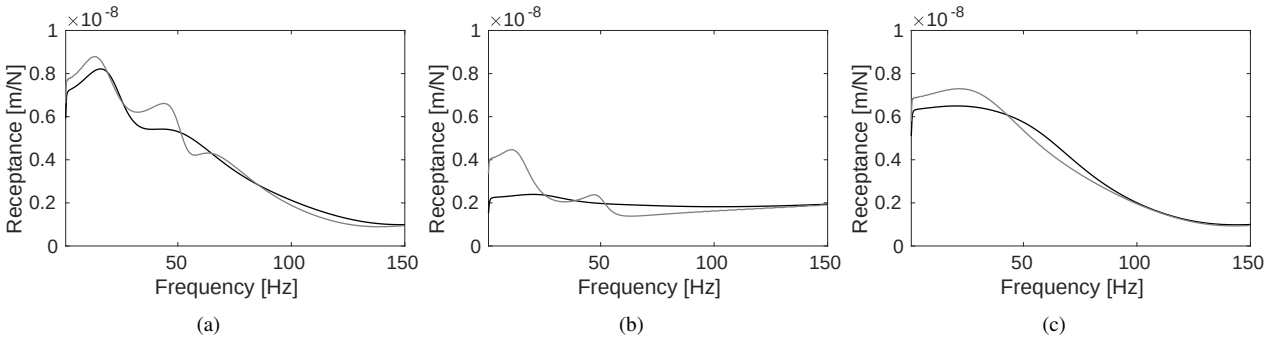

Figure 12: The displacement of the rail of the (a) ballasted track on an embankment, (b) slab track and (c) at-grade track, computed by (black line) the reference model and (grey line) the scoping model.

whereas the response of the slab track system is underestimated at mid frequency range. However, in general, considering the degree of input uncertainty for ground vibration models, the scoping model is within a reasonable range of accuracy.

Figure 14 presents the frequency contents in one-third octave bands of the dynamic load of an axle computed using both models. The estimation of the dynamic load from the proposed model coincides very strongly with those obtained using the reference model.

Figure 15 shows the frequency contents and the running RMS values of the free-field response, due to a S-100 train passage at $v = 100$ km/h. The running RMS value has been computed from the weighted acceleration with a time window of 1 s as prescribed by the ISO 2631 standard [2]. The discrepancies between models are low and in accordance with those observed in the mobility results (Figure 13). The running RMS curves present a similar agreement with differences in the range of $\{-4\,\mathrm{dB}, 1.5\,\mathrm{dB}\}$.

Overall there is strong agreement between the reference and scoping model with regard to receptance, mobility, dynamic load, frequency contents in one-third octave bands and running RMS values. This is true for the ballasted and slab tracks. Therefore it is concluded that the scoping model is capable of predicting train track forces.

3.2.2. Track-soil transfer function

The scoping model uses a NN to convert the Green's function for a soil into the response of a coupled track-soil system. To determine the accuracy of this approach, three homogenous soil cases were investigated, each corresponding to Eurocode 8 [37] (Table 1): soft, medium and stiff. Their exact properties are shown in Table 8, and the train speed used was $v = 100$ km/h.

Table 8: Homogeneous soil properties.

	h [m]	c_p [m/s]	c_s [m/s]	ξ [-]	ρ [kg/m^3]
Soft soil	∞	345.2	172.6	0.05	1800
Medium soil	∞	669.8	334.9	0.05	1800
Stiff soil	∞	993.6	496.8	0.05	1800

Figure 16 shows the influence of soil stiffness on the rail receptances from both models. The accuracy of the proposed

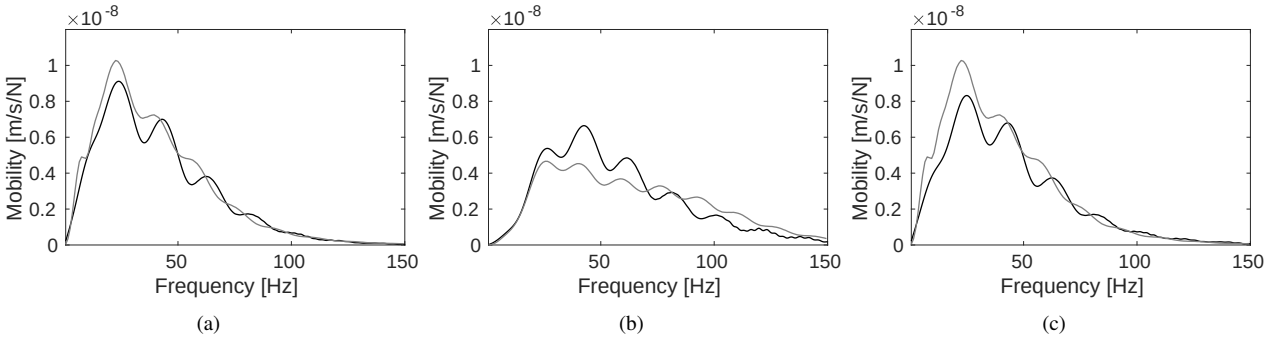

Figure 13: Free-field vertical mobility at a distance of 20 m from the (a) ballasted track on an embankment, (b) slab track and (c) at-grade track, computed by (black line) the reference model and (grey line) the scoping model.

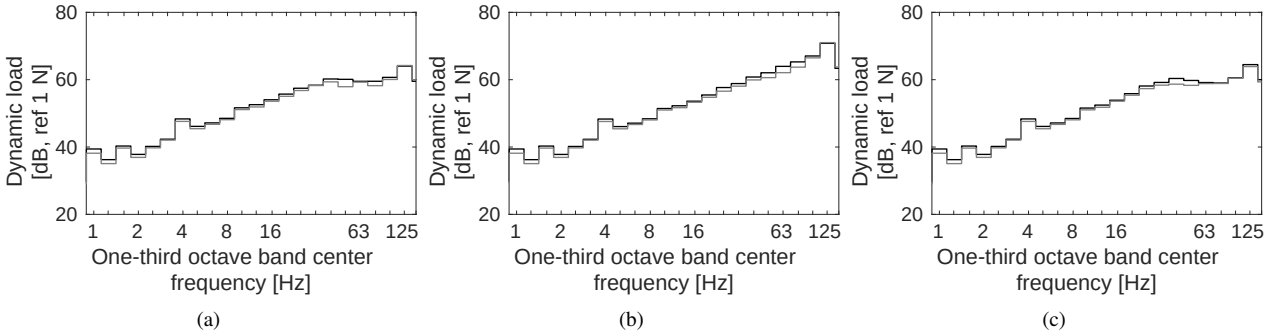

Figure 14: One-third octave band center frequency of the dynamic load of an axle with unsprung mass $m_s = 2048$ kg at $v = 100$ km/h for the (a) ballasted track on an embankment, (b) slab track and (c) at-grade track computed by (black line) the reference model and (grey line) the scoping model.

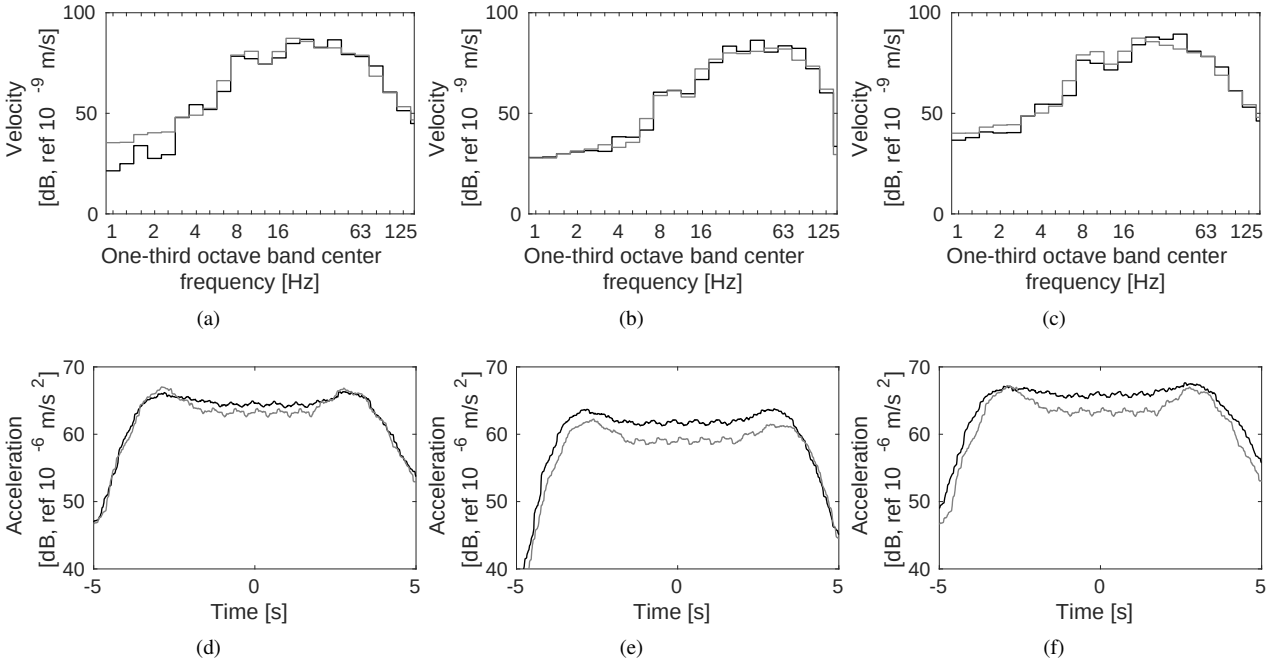

Figure 15: (a-c) One-third octave band center frequency of the vertical velocity and (d-f) running RMS value of the vertical weighted acceleration in the free-field at a distance of 20 m for the (a,d) ballasted track on an embankment, (b,e) slab track and (c,f) at-grade track due to a S-100 train passage at $v = 100$ km/h computed by (black line) the reference model and (grey line) the scoping model.

model in the estimations is good, particularly for the medium and stiff soils. There is some small discrepancy at low frequency for the soft soil, however in general accuracy seems relatively independent from soil stiffness.

Free-field mobilities at a distance of 20 m from the track are presented in Figure 17 for three homogeneous soils. Although there are some discrepancies between both prediction models, the magnitude and trend of results is good and it does not depend on soil stiffness.

The effect of soil stiffness on free-field vibrations due to the train passage is presented in Figure 18. According to the previous results (Figures 16 and 17), the frequency contents of the soil vibrations (Figure 18) show that the dominant frequencies due to the excitation vary from 10 to 40 Hz for the soft soil to 30 and 70 Hz for the stiff soil. The highest discrepancies between both models are concentrated in the lower frequencies.

A similar analysis to the presented in Section 3.2 was performed considering layered soils. However, the results are not included because the conclusions are the same as those obtained previously.

Bearing in mind the differences between both models are dependent on the soil stiffness, but these uncertainties do not follow a clear trend, it can be concluded that soil properties are important parameters for the accuracy of the scoping model predictions.

4. Analysis

This section presents a brief sensitivity analysis on the effect of track properties and train speed on vibration levels, as calculated using the scoping model.

Figure 19 shows the modulation of the dynamic loads and free-field response due to the track type. It can be seen that the dynamic slab track loads are higher at frequencies above 40 Hz. This is because the slab track had a higher stiffness which causes an increase of the free field response at the high frequency range. However, the soil response due to the train passage at the low and medium frequency ranges is attenuated by the slab track due to the effect of the free-field mobility (Figure 20).

Next, the scoping model was used to assess the effect of train speed on railway vibrations. Free-field response due to the passage of a S-100 train travelling at {100, 150 , 200} km/h on the generic ballasted track was analysed. A homogeneous medium soil with $c_s = 200$ m/s as described in the previous Section 3.2.1 was considered.

Figure 21 presents the influence of the train speed on the free-field predictions computed by the proposed model. The quasi-static contribution can be observed in the frequency content around the axle passing frequency $f_a = v/L_a = \{9.26, 13.9, 18.52\}$ Hz. The dominant frequency due to the dynamic excitation remains in the range between 20 and 40 Hz for the different train speeds. Both quasi-static and dynamic contributions increase with train speed, however it is more pronounced for the quasi-static case.

Finally, Figure 22 shows the relationship between train speed and the maximum transient vibration value (MTVV) [2] of the free field acceleration. The predicted vibration response has been weighted according to ISO2631 [2] to obtain the MTVV metric. A clear trend is observed with vibration levels increasing with train speed.

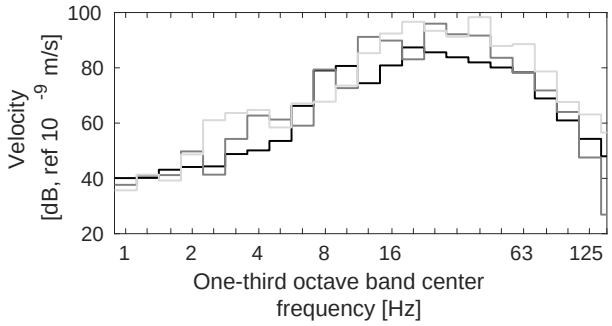

Figure 21: One-third octave band center frequency of the vertical velocity in the free-field due to a S-100 train passage at (black line) $v = 100$ km/h, (dark grey line) $v = 150$ km/h and (light grey line) $v = 200$ km/h at 20 m computed by the scoping model.

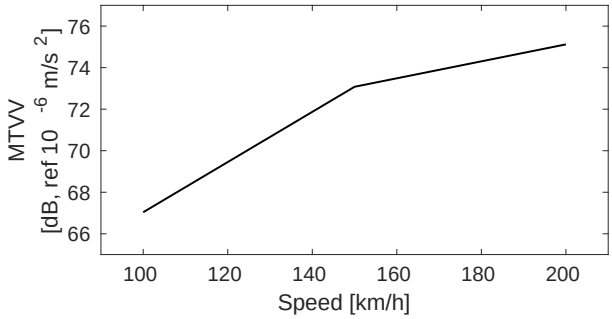

Figure 22: MTVV in the free-field due to a S-100 train passage at 20 m depending on the speed of train, computed by the scoping model.

5. V_{s30} parameter

V_{s30} is a measure of the mean shear wave speed in the top 30m of soil [37]. It is a property commonly used in earthquake engineering as an estimate of surface shear wave velocity. Databases of V_{s30} values exist that cover the entire earth's landmass, meaning that V_{s30} can potentially be used to increase the accuracy of desktop vibration scoping studies. However, a challenge is that the mean shear wave velocity over a 30m depth is typically higher than the shear wave speed at the uppermost soil surface (i.e. where ground-borne vibration is most efficient). Although the parameter V_{s30} is recognised in international standards [37, 60], there have been studies about its limitations [51, 61–63]. Therefore the accuracy of using V_{s30} to approximate layered soils, within a railway vibration setting was investigated.

To do so, results for each layered soil were compared with those obtained for a homogeneous soil considering $c_s = V_{s30}$.

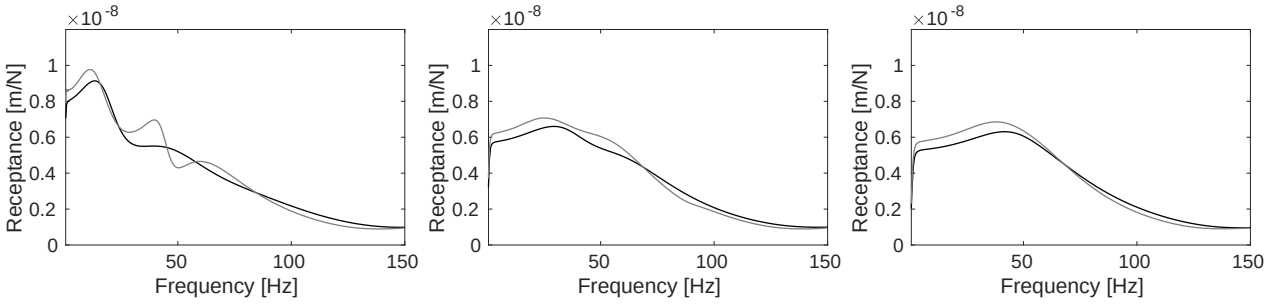

Figure 16: The displacement of the rail of the ballasted track for the homogeneous (a) soft, (b) medium and (c) stiff soils, computed by (black line) the reference model and (grey line) the scoping model.

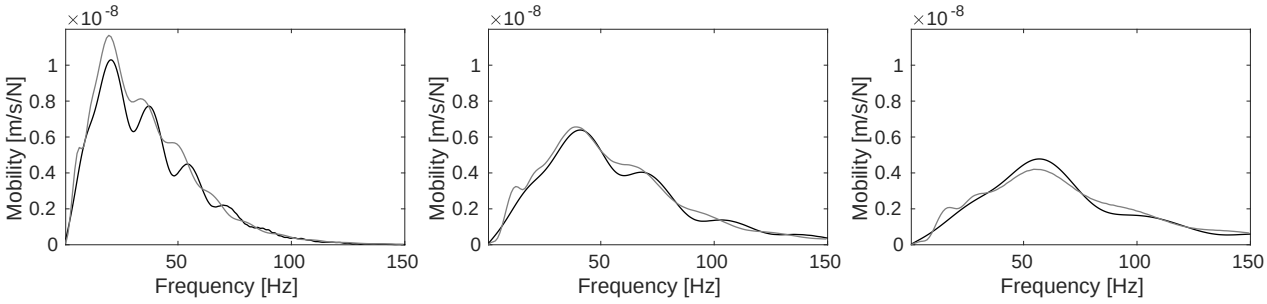

Figure 17: Free-field vertical mobility at 20 m of the ballasted track for the homogeneous (a) soft, (b) medium and (c) stiff soils, computed by (black line) the reference model and (grey line) the scoping model.

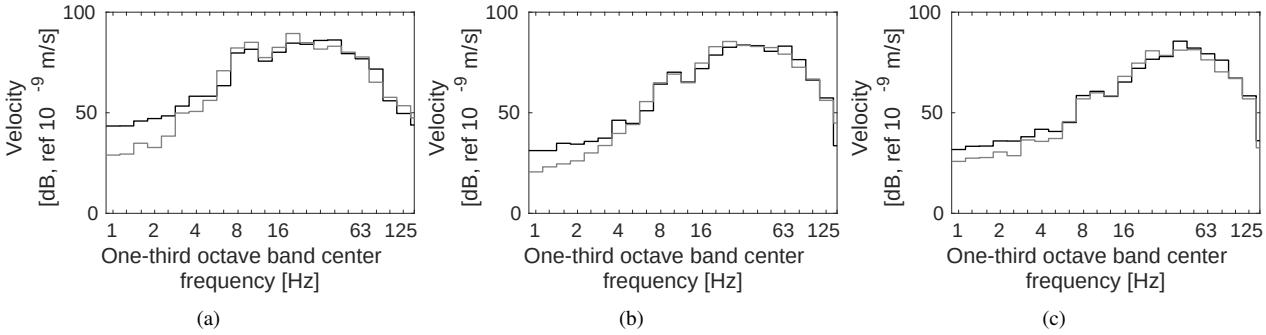

Figure 18: Frequency content of the vertical velocity at 20 m from the ballasted track due to a S-100 train passage at $v = 100$ km/h for the homogeneous (a) soft, (b) medium and (c) stiff soils, computed by (black line) the reference model and (grey line) the scoping model.

Hereafter the homogeneous soil with $c_s = V_{s30}$ is called equivalent homogeneous soil.

Figure 23 shows the rail receptances from the scoping model considering again the ballasted track (Table 2) for the three layered soils (Table 9) and the equivalent homogeneous soil. The layered soil properties were chosen to ensure the V_{s30} matched the c_s properties shown in Table 8. It is observed that peaks in the track response for the three layered soils are found in the frequency range 12 Hz to 16 Hz. This is because the dominant frequency is strongly dependent upon the properties of the uppermost soil layer, which are similar for the three layered soils. A better agreement in terms of peak amplitudes is obtained at high frequencies. Regarding the three different soils, the homogeneous approximation performs best for the soft soil. This is because it has a smoother soil stratigraphy, characterised by a smaller discrepancy between the upper and lower layers' stiffness.

Figure 24 shows the influence of soil stratigraphy on free-field mobility. In these results, it should be remembered that the neural network approach only utilises the upper layer properties (h_1 and c_{s_1}) and the V_{s30} parameter (Figure 2), meaning the full soil profile is not considered. Regarding mobility results the

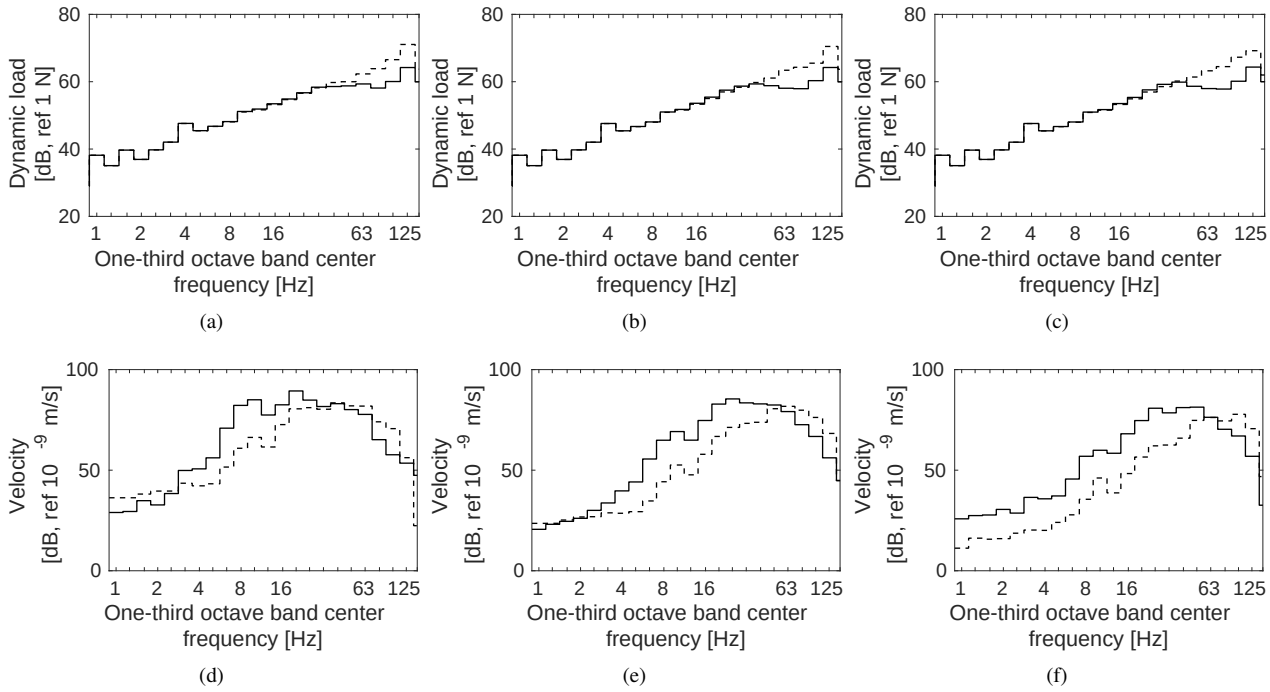

Figure 19: Frequency content of the (a-c) dynamic load of an axle with unsprung mass $m_s = 2048$ kg and (d-f) the vertical velocity in the free-field at 20 m from the track due to a S-100 train passage, at $v = 100$ km/h for the homogeneous (a,d) soft, (b,e) medium and (c,f) stiff soils (Table 8): (solid line) ballasted and (dashed line) slab tracks.

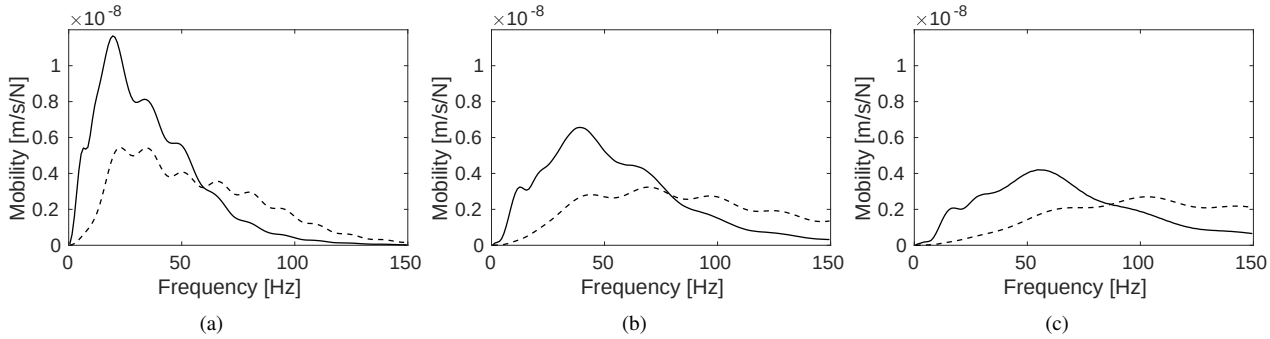

Figure 20: Free-field vertical mobility at 20 m from the track centerline for the homogeneous (a) soft, (b) medium and (c) stiff soils (Table 8): (solid line) ballasted and (dashed line) slab tracks.

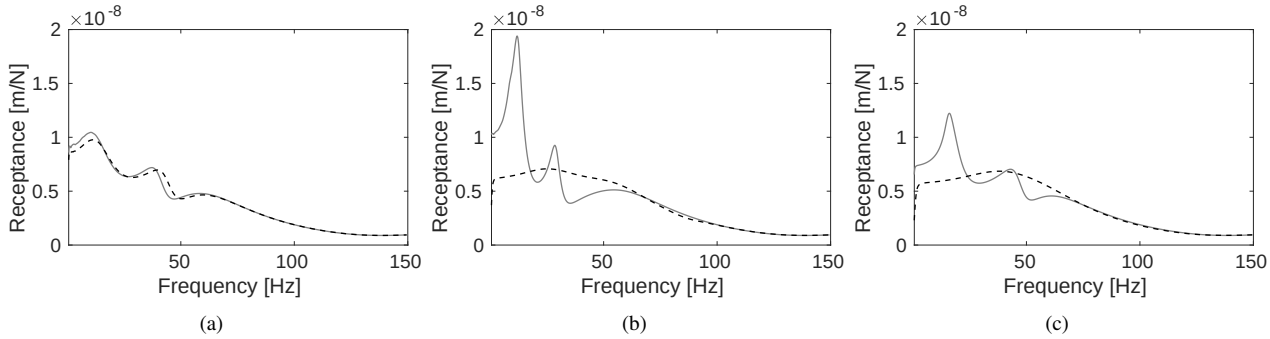

Figure 23: The displacement of the rail for the layered (a) soft, (b) medium and (c) stiff soils, computed by (grey line) the scoping model. Superimposed is the solution for (black dashed line) the equivalent homogeneous soil.

Table 9: Layered soil properties.

		h [m]	c_p [m/s]	c_s [m/s]	ξ [-]	ρ [kg/m^3]	V_{s30} [m/s]
Soft	Layer 1	24.1	318.9	159.5	0.05	1800	172.6
	Half-space	∞	518.1	259.1	0.05	1800	
Medium	Layer 1	1.7	220.9	110.5	0.05	1800	334.9
	Layer 2	7.8	479.4	239.7	0.05	1800	
	Layer 3	2.7	726	363	0.05	1800	
	Half-space	∞	1038	519	0.05	1800	
Stiff	Layer 1	2	361.5	180.7	0.05	1800	496.8
	Layer 2	3.6	660.4	330.2	0.05	1800	
	Layer 3	1.8	1113.2	556.6	0.05	1800	
	Half-space	∞	1291.6	645.8	0.05	1800	

level of error is similar to the receptance results, with the soft soil showing better agreement compared to the medium and stiff soils.

Figure 25 shows the free-field vibrations due to the S-100 train passage at $v = 100$ km/h computed from the proposed model. Some differences are seen for the soft and stiff soils at low frequencies, and medium and stiff soils in the mid frequency range. In general the agreement is reasonable, although at some frequencies there are errors of up to 14 dB.

Figure 26 presents the MTVV value [2] at different distances from the ballasted track, considering different V_{s30} values. The response for homogeneous soils decrease as the soil stiffness increase as expected, however, the layered soils show the opposite behaviour. This is due to the shear wave velocity of the upper layer in each soil (Table 9). In all cases, this shear wave velocity is lower than the V_{s30} parameter and the difference between both increases from the soft to the stiff soil. The soil response is higher for the stiff layered soil since the free-field response is mainly influenced by surface waves. Therefore, it can be concluded that characterising soils using the V_{s30} parameter should be performed carefully and only for cases with straightforward stratigraphies.

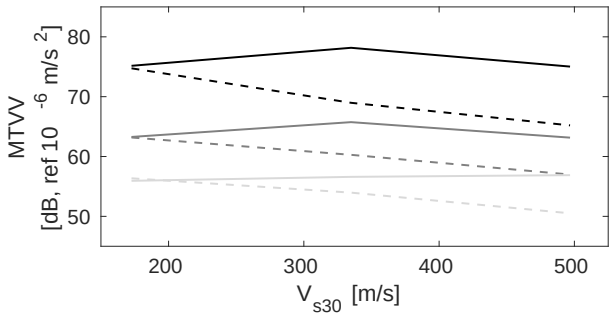

Figure 26: MTVV in the free-field at distances from the ballasted track of (black line) 10 m, (dark grey line) 30 m and (light grey line) 50 m due to a S-100 train passage at $v = 100$ km/h considering (solid lines) layered and (dashed lines) homogeneous soils characterized by their V_{s30} parameter.

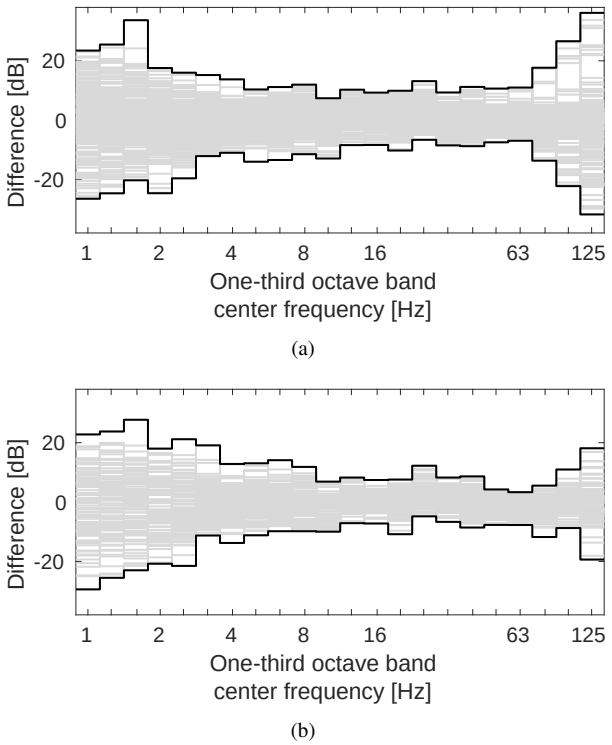

Figure 27: (Grey lines) one-third octave band center frequency of the differences Δv for all the cases of the (a) ballasted and (b) slab tracks. (Black lines) superimposed is the envelope of the highest discrepancies.

6. Discussion

Quantification of scoping model accuracy is challenging because of limited field data and the unknown error levels inherent within the reference model. Therefore, in an attempt to make a global comparison, Figure 27 shows the discrepancy between scoping and reference model results, for all the cases previously presented in this study. The error was calculated as $\Delta v = 20\log_{10}\left(v^P/v^R\right)$, where v^P and v^R were the response from the scoping and the reference model respectively.

Regarding the ballasted tracks, the at-grade and embankment results have been combined, and shown with superimposed envelope curves. It is seen that prediction ability is better in the mid frequency range. As for the slab track, best performance is also in the mid-frequency range.

The global uncertainty of the scoping model was determined using the MTVV vibration metric [2]. Figure 28 presents the response for all the cases. A good agreement is found with differences mainly found between −4.8 dB to 5.6 dB. Therefore the accuracy is similar to the uncertainty range between 5 dB to 20 dB as found in previous research [54, 64, 65].

A dataset of 4410000 data points was used to create the NN model. A discussion on the minimum number of data points needed to achieve sufficient NN model accuracy is important

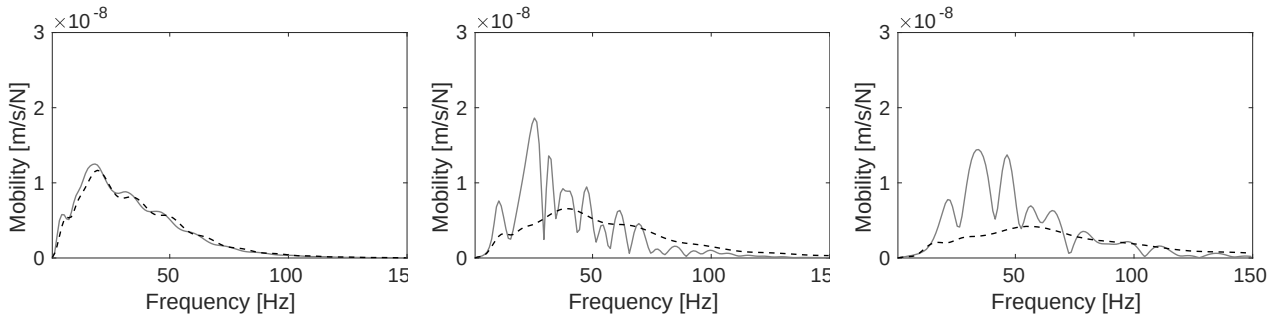

Figure 24: Free-field vertical mobility at 20 m for the layered (a) soft, (b) medium and (c) stiff soils, computed by (grey line) the scoping model. (Black dashed line) superimposed is the solution for the equivalent homogeneous soil.

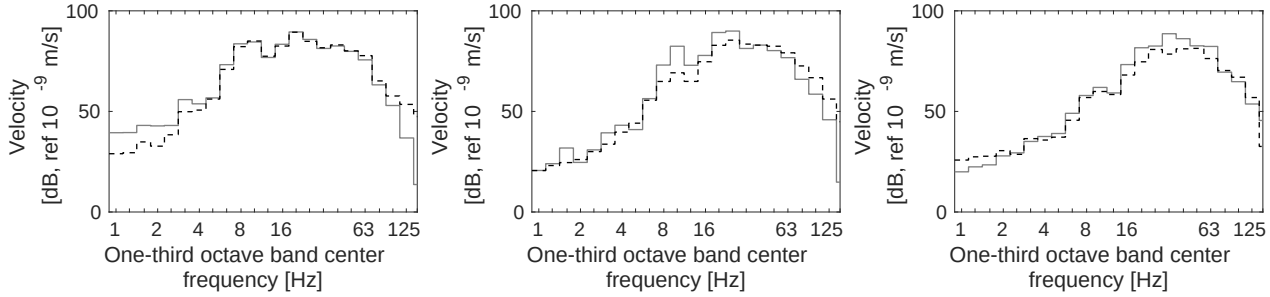

Figure 25: One-third octave band center frequency of the vertical velocity in the free-field due to a S-100 train passage at v = 100 km/h at 20 m for the layered (a) soft, (b) medium and (c) stiff soils, computed by (grey line) the scoping model. (Black dashed line) superimposed is the solution for the equivalent homogeneous soil.

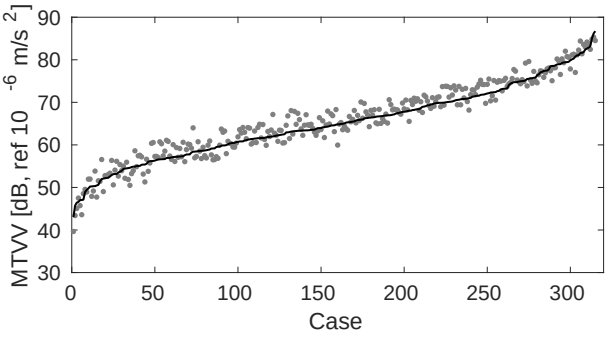

Figure 28: MTVV in the free-field due to a S-100 train passage at 20 m for all the cases, computed by (black line) the reference model and (grey points) the scoping model.

if it is to be developed for other cases (e.g. tracks, soil conditions, embankment types, etc.). Figure 29 shows the predictions for all the cases computed using the scoping model with a NN approach trained with four times the number of original data points (120 soil types × 5 distances × 150 frequencies × 196 wavenumbers = 17640000) and the reference model. The larger dataset required a significant increase in computation effort, however results did not improve. Therefore is concluded that increasing the number of data points does not signify a more accuracy model.

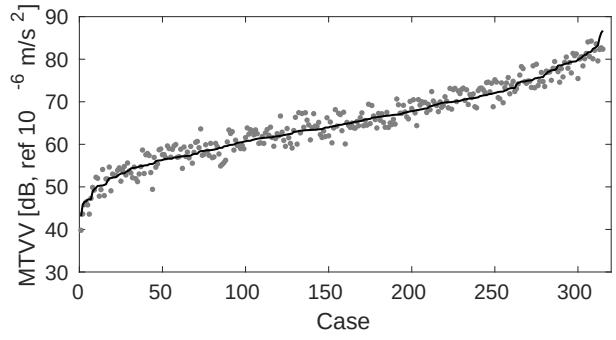

Figure 29: MTVV in the free-field due to a S-100 train passage at 20 m for all the cases, computed by (black line) the reference model and (grey points) the scoping model with a NN approach trained with four times of the original data points.

An important advantage of the new scoping model compared to alternative models is its computational efficiency. Table 10 shows the computational costs to obtain the free-field response for a S-100 train travelling at v = 100 km/h using an `Intel One Core i7@1.87` GHz computer. The run times refer to the source-propagation problem of waves in the soil. The running time does not depend on the soil's properties. Taking into ac-

count the architecture of the scoping and reference models (Figures 1 and 11), Table 10 outlines the main calculation steps and their run times. It should be noted that:

- The time required to calculate the track-soil transfer function $\tilde{\mathbf{u}}_{\mathrm{ff}}$ (step 2.1) using the scoping model was primarily due to the evaluation of the soil Green's function (step 2.1.2). The estimation of the correction factor $\tilde{A}_g$ through the NN approach (step 2.1.1) required minimal cost. The combination of these two steps resulted in a run time that was lower than that for the reference model which relied on a FEM-BEM formulation.
- The simplified track model (Figure 5) allowed the scoping model to reduce computations of train-track excitations $\mathbf{g}$ (step 2.2) since the soil-track interaction was represented by a spring-damper element. Again, the reference model used a BEM-FEM methodology to calculate the train-track excitations and track-soil transfer function $\tilde{\mathbf{u}}_{\mathrm{ff}}$, thus requiring additional computation.
- Running times for obtaining free-field predictions are identical.
- Moreover, the preprocessing in the scoping model involves a minimal time.

Table 10: Average running time.

Step	Reference model	Scoping model
Track-soil transfer function	15 min	5 min
Train-track forces	25 min	38 s
Free-field predictions	30 s	30 s

Considering these much reduced computational requirements, strong accuracy and the versatility of the proposed scoping model, it is concluded that it could be a powerful tool during the early design stages of railway lines.

7. Conclusions

In this work, a simplified methodology to compute the propagation of railway vibrations from track to free-field was presented. The model is novel because it is able to simulate the generation, propagation and immission of vibrations, for complex vehicle, track and soil arrangements in minimal time. To do so, a 2.5D FEM track model was combined with a hybrid direct stiffness-neural network procedure to create an overall model describing the vehicle-track-soil problem.

To validate the model, a combination of experimental and numerical data was used. Track receptance, free-field mobility and soil vibration due to train passage were analysed and the new model was found to have strong prediction ability.

A sensitivity analysis was undertaken using the validated model. Track type and train speed effects were compared and it was found that there was a strong relationship between vibration levels and both soil properties and track type. Also, comparisons were made to determine the accuracy of using a global database of V_{s30} soil properties to predict vibration levels. It was found that this simplification was only satisfactory for cases with smooth stratigraphies.

Acknowledgements

This research was funded by the Spanish Ministry of Economy and Competitiveness (Ministerio de Economía y Competitividad) through research project BIA2016-75042-C2-1-R. Financial support is gratefully acknowledged. The support given by the Andalusian Scientific Computing Centre (CICA) and the Leverhulme Trust (UK) is also gratefully acknowledged.

The first author would like to thank the Spanish Ministry of Education, Culture and Sport (Ministerio de Educación, Cultura y Deporte) for the financial support of his research stay at the School of Civil Engineering of the University of Leeds through the scholarship "Salvador de Madariaga" Reference PRX18/00115.

References

[1] D.P. Connolly, G.P. Marecki, G. Kouroussis, I. Thalassinakis, P.K. Woodward, The growth of railway ground vibration problems – A review, Science of the Total Environment (2015) http://dx.doi.org/10.1016/j.scitotenv.2015.09.101.

[2] International Organization for Standardization, ISO 2631-1:2003: Mechanical vibration and shock–Evaluation of human exposure to whole-body vibration–Part 1: General requirements (2003).

[3] International Organization for Standardization, ISO 2631-2:2003: Mechanical vibration and shock–Evaluation of human exposure to whole-body vibration–Part 2: Vibration in buildings (1–80 Hz) (2003).

[4] International Organization for Standardization, ISO 14837-1:2005 Mechanical vibration–Ground-borne noise and vibration arising from rail systems–Part 1: General guidance (2005).

[5] L. Auersch, A. Romero, P. Galvín, Respuesta dinámica de edificaciones producida por campos de onda incidentes considerando la interacción suelo-estructura, Revista Internacional de Métodos Numéricos para Cálculo y Diseño en Ingeniería 30 (4) (2014) 256–263.

[6] P. Galvín, J. Domínguez, High-speed train-induced ground motion and interaction with structures, Journal of Sound and Vibration 307 (2007) 755–777.

[7] H. Xia, Y.M. Cao, G. De Roeck, Theoretical modeling and characteristic analysis of moving-train induced ground vibrations, Journal of Sound and Vibration 329 (2010) 819–832.

[8] P. Galvín, A. Romero, J. Domínguez, Fully three-dimensional analysis of high-speed train–track–soil–structure dynamic interaction, Journal of Sound and Vibration 329 (2010) 5147–5163.

[9] P. Lopes, P. Alves Costa, M. Ferraz, R. Calçada, A. Silva Cardoso, Numerical modeling of vibrations induced by railway traffic in tunnels: From the source to the nearby buildings, Soil Dynamics and Earthquake Engineering 61–62 (2014) 269–285.

[10] G. Lombaert, G. Degrande, J. Kogut, S. François, The experimental validation of a numerical model for the prediction of railway induced vibrations, Journal of Sound and Vibration 297 (3) (2006) 512 – 535. doi:https://doi.org/10.1016/j.jsv.2006.03.048.

[11] G. Lombaert, G. Degrande, Ground-borne vibration due to static and dynamic axle loads of intercity and high-speed trains, Journal of Sound and Vibration 319 (3–5) (2009) 1036–1066. doi:http://dx.doi.org/10.1016/j.jsv.2008.07.003.

[12] L. Auersch, The excitation of ground vibration by rail traffic: theory of vehicle–track–soil interaction and measurements on high-speed lines, Journal of Sound and Vibration 284 (2005) 103–132.

[13] X. Sheng, C.J.C. Jones, D.J. Thompson, Prediction of ground vibration from trains using the wavenumber finite and boundary element methods, Journal of Sound and Vibration 293 (2006) 575–586.

[14] P. Galvín, S. François, M. Schevenels, E. Bongini, G. Degrande, G. Lombaert, A 2.5d coupled fe-be model for the prediction of railway induced vibrations, Soil Dynamics and Earthquake Engineering 30 (12) (2010) 1500 – 1512. doi:https://doi.org/10.1016/j.soildyn.2010.07.001.

[15] S. François, M. Schevenels, P. Galvín, G. Lombaert, G. Degrande, A 2.5d coupled fe–be methodology for the dynamic interaction between longitudinally invariant structures and a layered halfspace, Computer Methods in Applied Mechanics and Engineering 199 (23) (2010) 1536 – 1548. doi:https://doi.org/10.1016/j.cma.2010.01.001.

[16] P. Alves Costa, R. Calçada, A. Silva Cardoso, Track–ground vibrations induced by railway traffic: In-situ measurements and validation of a 2.5D FEM-BEM model, Soil Dynamics and Earthquake Engineering 32 (2012) 111–128.

[17] A. Romero, A. Tadeu, P. Galvín, J. António, 2.5D coupled BEM–FEM used to model fluid and solid scattering wave, International Journal for Numerical Methods in Engineering 101 (2015) 148–164.

[18] A. Romero, P. Galvín, J. António, J. Domínguez, A. Tadeu, Modelling of acoustic and elastic wave propagation from underground structures using a 2.5d bem-fem approach, Engineering Analysis with Boundary Elements 76 (2017) 26 – 39. doi:http://dx.doi.org/10.1016/j.enganabound.2016.12.008.

[19] P. Jean, C. Guigou, M. Villot, A 2.5D BEM Model for Ground-Structure Interaction, Building Acoustics 11 (3) (2004) 1–17.

[20] J.T. Nelson, H.J. Sauernman, A prediction procedure for rail transportation groundborne noise and vibration, Transportation Research Record: Journal of the Transportation Research Board 1143 (1987) 26–35.

[21] C. Madshus, B. Bessason, L. Harvik, Prediction model for low frequency vibration from high speed railways on soft ground, Journal of Sound and Vibration 193 (1) (1996) 195–203.

[22] F. Rossi, A. Nicolini, A simple model to predict train-induced vibration: theoretical formulation and experimental validation, Enviornmental Impact Assesment Review 23 (2003) 305–322.

[23] C. With, M. Bahrekazemi, A. Bodare, Validation of an empirical model for prediction of train-induced ground vibrations, Soil Dynamics and Earthquake Engineering 26 (2006) 983–990.

[24] C.E. Hanson, D.A. Towers, L.D. Meister, High-speed ground Transportation Noise and Vibration Impact Assessment, HMMH Report 293630-4, U.S. Department of Transportation, Federal Railroad Administration, Office of Railroad Development.

[25] C.E. Hanson, D.A. Towers, L.D. Meister, Transit Noise and Vibration Impact Assessment, Report FTA-VA-90-1003-06, U.S. Department of Transportation, Federal Transit Administration, Office of Planning and Environment.

[26] H. Verbraken, G. Lombaert, G. Degrande, Verification of an empirical prediction method for railway induced vibrations by means of numerical simulations, Journal of Sound and Vibration 330 (8) (2011) 1692–1703.

[27] M. Hussein, H. Hunt, K. Kuo, P. Alves Costa, J. Barbosa, The use of sub-modelling technique to calculate vibration in buildings from underground railways, Proceedings of the Institution of Mechanical Engineers, Part F: Journal of Rail and Rapid Transit 229 (3) (2013) 303 – 314. doi:https://doi.org/10.1177/0954409713511449.

[28] G. Kouroussis, L. V. Parys, C. Conti, O. Verlinden, Prediction of ground vibrations induced by urban railway traffic: An analysis of the coupling assumptions between vehicle, track, soil, and buildings, The International Journal of Acoustics and Vibration 18 (4) (2013) 163 – 172. doi:https://doi.org/10.20855/ijav.2013.18.4330.

[29] D.P. Connolly, G. Kouroussis, A. Giannopoulos, O. Verlinden, P.K. Woodward, M.C. Forde, Assesment of railway vibrations using an efficient scoping model, Soil Dynamics and Earthquake Engineering 58 (2014) 37–47.

[30] D.P. Connolly, G. Kouroussis, P.K. Woodward, A. Giannopoulos, O. Verlinden, M.C. Forde, Scoping prediction of re-radiated ground-borne noise and vibration near high speed rails lines with variable soils, Soil Dynamics and Earthquake Engineering 66 (2014) 78–88.

[31] A. Triepaischajonsak, D.J. Thompson, A hybrid modelling approach for predicting ground vibration from trains, Journal of Sound and Vibration 335 (2015) 147 – 173. doi:http://dx.doi.org/10.1016/j.jsv.2014.09.029.

[32] E. Kausel, J. M. Roësset, Stiffness matrices for layered soils, Bulletin of the Seismological Society of America 71 (6) (1981) 1743.

[33] K. Kuo, H. Verbraken, G. Degrande, G. Lombaert, Hybrid predictions of railway induced ground vibration using a combination of experimental measurements and numerical modelling, Journal of Sound and Vibration 373 (2016) 263–284.

[34] G. Kouroussis, K.E. Vogiatzis, D.P. Connolly, A combined numerical/experimental prediction method for urban railway vibration, Soil Dynamics and Earthquake Engineering 97 (2017) 377 – 386. doi:http://dx.doi.org/10.1016/j.soildyn.2017.03.030.

[35] E. Kausel, Fundamental solutions in elastodynamics: a compendium, Cambridge University Press, 2006.

[36] M. Schevenels, S. François, G. Degrande, Edt: An elastodynamics toolbox for MATLAB, Computers & Geosciences 35 (8) (2009) 1752 – 1754. doi:http://dx.doi.org/10.1016/j.cageo.2008.10.012.

[37] European Committee for Standardization, Eurocode 8: Design of structures for earthquake resistance–Part 1 : General rules, seismic actions and rules for buildings (1998).

[38] C.R. Arjun, A. Kumar, Neural network estimation of duration of strong ground motion using japanese earthquake records, Soil Dynamics and Earthquake Engineering 31 (2011) 866–872.

[39] C. Hung, S. Ni, Using multiple neural networks to estimate the screening effect of surface waves by in-filled trenches, Computers and Geotechnics 34 (2007) 397–409.

[40] K. Kuźniar, Z. Waszczyszyn, Neural analysis of vibration problems of real flat buildings and data pre-processing, Engineering Structures 24 (2002) 1327–1335.

[41] K. Kuźniar, E. Maciąg, Z. Waszczyszyn, Computation of response spectra from mining tremors using neural networks, Soil Dynamics and Earthquake Engineering 25 (2005) 331–339.

[42] J. Shu, Z. Zhang, I. Gonzalez, R. Karoumi, The application of a damage detection method using artificial neural network and train-induced vibrations on a simplified railway bridge model, Engineering Structures 52 (2013) 408–421.

[43] D. E. Rumelhart, J. L. McClelland, Parallel distributed processing: Explorations in the microstructure of cognition. Vol 1, MIT Press, Cambridge, MA, 1986.

[44] M. H. Beale, M. T. Hagan, H. B. Demuth, Neural network toolbox User's guide, Mathworks, Inc, 2017.

[45] Y. L. Cun, I. Kanter, S. A. Solla, Second order properties of error surfaces: Learning time and generalization, Advances in Neural Information Processing Systems 3 (1991) 918–924.

[46] M. T. Hagan, M. B. Menhaj, Training feedforward networks with the marquardt algorithm, EEE Transactions on Neural Networks 5 (6) (1994) 989–993.

[47] M. Monjezi, M. Ahmadi, M. Sheikhan, A. Bahrami, A. R. Salimi, Predicting blast-induced ground vibration using various types of neural networks, Soil Dynamics and Earthquake Engineering 30 (2010) 1233–1236.

[48] V. Nourani, M. S. Fard, Sensitivity analysis of the artificial neural network outputs in simulation of the evaporation process at different climatologic regimes, Advances in Engineering Software 47 (2012) 127–146.

[49] M. Yurdakul, H. Akdas, Modeling uniaxial compressive strength of building stones using non-destructive test results as neural networks input parameters, Construction and Building Materials 47 (2013) 1010–1019.

[50] J. Shi, Reducing prediction error by transforming input data neural networks, Journal of Computing in Civil Engineering 14 (2) (2000) 109 – 116. doi:https://doi.org/10.1061/(ASCE)0887-3801(2000)14:2(109).

[51] V.W. Lee, M.D. Triufnac, Should average shear-wave velocity in the top 30 m of soil be used to describe seismic amplification?, Soil Dynamics and Earthquake Engineering 30 (2010) 1250–1258.

[52] B. Olivier, D. P. Connolly, P. A. Costa, G. Kouroussis, The effect of embankment on high speed rail ground vibrations, International Journal of Rail Transportation 4 (4) (2016) 229–246. doi:10.1080/23248378.2016.1220844.

[53] S. B. Mezher, D. P. Connolly, P. K. Woodward, O. Laghrouche, J. Pombo, P. A. Costa, Railway critical velocity – analytical prediction and analysis, Transportation Geotechnics 6 (2016) 84 – 96. doi:https://doi.org/10.1016/j.trgeo.2015.09.002.

[54] G. Lombaert, P. Galvín, S. François, G. Degrande, Quantification of uncertainty in the prediction of railway induced ground vibration due to the use of statistical track unevenness data, Journal of Sound and Vibration 333 (18) (2014) 4232 – 4253. doi:https://doi.org/10.1016/j.jsv.2014.04.052.

[55] I. 8608, Mechanical vibration – road surface profiles – Reporting of measured data, International Organization for Standardization, 1995.

[56] H.Braun, T.Hellenbroich, Messergebnisse von strassenunebenheiten, VDI Berichte 877 (1991) 47–80.
[57] D. López-Mendoza, A. Romero, D. Connolly, P. Galvín, Scoping assessment of building vibration induced by railway traffic, Soil Dynamics and Earthquake Engineering 93 (2017) 147–161. doi:http://dx.doi.org/10.1016/j.soildyn.2016.12.008.
[58] Deutsches Institut für Normung, DIN 45672 Teil 2: Schwingungsmessungen in der Umgebung von Schienenverkehrswegen: Auswerteverfahren (1995).
[59] P. Alves Costa, A. Colaço, R. Calçada, A. Silva Cardoso, Critical speed of railway tracks. Detailed and simplified approaches, Transportation Geotechnics 2 (2015) 30–46.
[60] Building Seismic Safety Council, NEHRP Recommended Seismic Provisions for New Buildings and Other Structures, FEMA P-1050 (2015).
[61] L.A. Wald, J. Mori, Evaluation of methods for estimating linear site-response amplifications in the los angeles region, Bulletin of the Seismological Society of America 90 (6B) (2000) S32–S42.
[62] S. Castellaro, F. Mulargia, P.L. Rossi, Vs30: Proxy for seismic amplification?, Seismological Research Letters 79 (4) (2008) 540–543.
[63] L.A. Wald, J. Mori, Comparisons between V_{S30} and spectral response for 30 sites in newcastle, australia, from collocated seismic cone penetrometer, active- and passive-source V_S data, Bulletin of the Seismological Society of America 106 (4) (2016) 1690–1709.
[64] S. Jones, K. Kuo, M.F.M. Hussein, H.E.M Hunt, Prediction uncertainties and inaccuracies resulting from common assumptions in modelling vibration from underground railways, Proceedings of the Institution of Mechanical Engineers, Part F: Journal of Rail and Rapid Transit 226 (2012) 501–512.
[65] D.P. Connolly, P. Alves Costa, G. Kouroussis, P. Galvín, P.K. Woodward, O. Laghrouche, Large scale international testing of railway ground vibrations across Europe, Soil Dynamics and Earthquake Engineering 71 (2015) 1–12.